

**BİR KANAT PROFİLİNDE AKIŞIN UYARDIĞI
YUNUSLAMA SALINIMLARI**

YÜKSEK LİSANS TEZİ
Uzay Müh. Egemen TİNAR

(708021005)

Tezin Enstitüye Verildiği Tarih : 9 Mayıs 2005
Tezin Savunulduğu Tarih : 2 Haziran 2005

Tez Danışmanı : Yrd. Doç. Dr. N. L. Okşan ÇETİNER YILDIRIM

Diğer Jüri Üyeleri : Prof. Dr. Fevzi ÜNAL

Doç. Dr. Fırat Oğuz EDİS

HAZİRAN 2005

ACKNOWLEDGEMENTS

First, I would like to thank my supervisor Asst. Prof. Dr. Okşan Çetiner - Yıldırım for her guidance and support throughout my studies at ITU.

I would like to extend my thanks to my friend Murat Sarıtaş, for the ideas he shared with me and the VI's, he wrote for this study. I am also thankful to staff of Trisonic Research Center, for giving me hand when I need.

Finally, I would like to express my gratitude to my family, I will forever be grateful to my family for their endless support and everything they have done for me.

May 2005

Egemen TINAR



CONTENTS

LIST OF TABLES	v
LIST OF FIGURES	vi
LIST OF SYMBOLS	ix
SUMMARY	x
ÖZET	xi
1. INTRODUCTION	1
2. LITERATURE REVIEW	3
3. EXPERIMENTAL SETUP	7
3.1. Wind Tunnel	7
3.1.1. Flow speed measurement	7
3.2. Airfoil and Mounting	9
3.3. Accelerometer	11
3.4. Laser and Camera	11
3.5. Seeding	12
3.6. Data Acquisition	12
3.7. Post Process	14
4. RESULTS	18
4.1. Wind Tunnel Performance	18
4.1.1. Pressure transducer validation	18
4.1.2. Flow speed measurement via PIV	20
4.2. Structural Properties of the System	23
4.3. Self-Induced Pitching Oscillations	24
4.3.1. Parameters of the study	24
4.3.2. Acceleration measurements	25
4.3.3. PIV measurements and vortex formation around the airfoil	28
5. CONCLUDING REMARKS	32
REFERENCES	34
APPENDIX A	37

APPENDIX B1	38
APPENDIX B2	47
APPENDIX B3	56
CURRICULUM VITAE	61



LIST OF TABLES

	<u>Page No.</u>
Table 4.1. Comparison of the results obtained by the transducers	20
Table 4.2. Stability data of the freestream velocity	20
Table 4.3. Velocity vectors obtained by PIV	22
Table 4.4. Velocity values obtained by Pitot static tube measurements	22
Table 4.5. Structural parameters of the airfoil-spring systems	24
Table 4.6. Cases of the study and corresponding values of the parameters	26



LIST OF FIGURES

	<u>Page No.</u>
Figure 3.1 : Side view of the 50x50 LSWT	8
Figure 3.2 : View of the 50x50 LSWT with the ventilation unit	8
Figure 3.3 : Pictures showing airfoil, its mounting and angle of attack mechanism from different angles of view.....	9
Figure 3.4 : Springs used in the study	10
Figure 3.5 : Experimental Setup of the study	10
Figure 3.6 : PCB Accelerometer, conditioner and mounting	11
Figure 3.7 : Schematic of PIV processes and components used in the study ..	13
Figure 3.8 : Time diagram of PIV system	14
Figure 3.9 : Raw PIV image and the top-hat filtered version of the same image.....	16
Figure 3.10 : Velocity fields obtained from the raw image and the filtered image	16
Figure 3.11 : Range validated velocity field and the remainig bad vectors	17
Figure 3.12 : Cleaned velocity field by V3 and the result after the NFILVB process	17
Figure 4.1 : Positioning of the Pitot static tube	19
Figure 4.2 : Positions of the Pitot static tube and captured flow field relative to each other	21
Figure 4.3 : A sample velocity field and indexes of the vectors in the vector field	21
Figure 4.4 : Decay of the impulse given to the system	24
Figure 4.5 : Pitching frequencies with respect to Reynolds number.....	27
Figure B1.1 : Time traces of acceleration for a period of 5 seconds. (Spring 1).	39
Figure B1.2 : Time traces of acceleration for a period of 5 seconds. (Spring 2).	40
Figure B1.3 : Time traces of acceleration for a period of 5 seconds. (Spring 3).	41
Figure B1.4 : Time traces of acceleration for a period of 1 second. (Spring 1)..	42
Figure B1.5 : Time traces of acceleration for a period of 1 second. (Spring 2)..	43
Figure B1.6 : Time traces of acceleration for a period of 1 second. (Spring 3)..	44
Figure B1.7 : Spectra of acceleration.....	45
Figure B1.8 : Spectra of acceleration (Frequency axis is non-dimensionalized	

	with corresponding reduced frequencies).....	46
Figure B2.1	: Selected 3 images of vorticity patterns for oscillations at $Re=75,189$ with Spring 1 ($\alpha_{init}=Angle\ 2$) a) $\alpha_{inst}=24^\circ$ b) $\alpha_{inst}=27^\circ$ c) $\alpha_{inst}=20^\circ$ d) $\alpha_{inst}=-3^\circ$ and corresponding acceleration–time trace (e) and acceleration spectra (f) graphs.....	48
Figure B2.2	: Selected 3 images of vorticity patterns for oscillations at $Re=147,725$ with Spring 1 ($\alpha_{init}=Angle\ 2$) a) $\alpha_{inst}=10^\circ$ b) $\alpha_{inst}=16^\circ$ c) $\alpha_{inst}=12^\circ$ d) $\alpha_{inst}=-4^\circ$ and corresponding acceleration–time trace (e) and acceleration spectra (f) graphs...	49
Figure B2.3	: Selected 3 images of vorticity patterns for oscillations at $Re=70,218$ with Spring 2 ($\alpha_{init}=Angle\ 2$) a) $\alpha_{inst}=8^\circ$ b) $\alpha_{inst}=10^\circ$ c) $\alpha_{inst}=14^\circ$ d) $\alpha_{inst}=15^\circ$ e) $\alpha_{inst}=12^\circ$ f) $\alpha_{inst}=-1^\circ$ and corresponding acceleration–time trace (g) and acceleration spectra (h) graphs...	50
Figure B2.4	: Selected 3 images of vorticity patterns for oscillations at $Re=147,869$ with Spring 2 ($\alpha_{init}=Angle\ 2$) a) $\alpha_{inst}=11^\circ$ b) $\alpha_{inst}=18^\circ$ c) $\alpha_{inst}=22^\circ$ d) $\alpha_{inst}=16^\circ$ e) $\alpha_{inst}=-2^\circ$ and corresponding acceleration–time trace (f) and acceleration spectra (g) graphs...	51
Figure B2.5	: Selected 3 images of vorticity patterns for oscillations at $Re=74,512$ with Spring 3 ($\alpha_{init}=Angle\ 2$) a) $\alpha_{inst}=17^\circ$ b) $\alpha_{inst}=23^\circ$ c) $\alpha_{inst}=21^\circ$ d) $\alpha_{inst}=-3^\circ$ and corresponding acceleration–time trace (e) and acceleration spectra (f) graphs.....	52
Figure B2.6	: Selected 3 images of vorticity patterns for oscillations at $Re=110,762$ with Spring 3 ($\alpha_{init}=Angle\ 2$) a) $\alpha_{inst}=10^\circ$ b) $\alpha_{inst}=18^\circ$ c) $\alpha_{inst}=19^\circ$ d) $\alpha_{inst}=13^\circ$ e) $\alpha_{inst}=-4^\circ$ and corresponding acceleration–time trace (f) and acceleration spectra (g) graphs...	53
Figure B2.7	: Selected 3 images of vorticity patterns for oscillations at $Re=76,063$ with Spring 3 ($\alpha_{init}=Angle\ 1$) a) $\alpha_{inst}=14^\circ$ b) $\alpha_{inst}=15^\circ$ c) $\alpha_{inst}=12^\circ$ d) $\alpha_{inst}=4^\circ$ and corresponding acceleration–time trace (e) and acceleration spectra (f) graphs.....	54
Figure B2.8	: Selected 3 images of vorticity patterns for oscillations at $Re=110,072$ with Spring 3 ($\alpha_{init}=Angle\ 1$) a) $\alpha_{inst}=11^\circ$ b) $\alpha_{inst}=12^\circ$ c) $\alpha_{inst}=10^\circ$ d) $\alpha_{inst}=7^\circ$ and corresponding acceleration–time trace (e) and acceleration spectra (f) graphs...	55
Figure B3.1	: Vorticity formation around the airfoil for one period of oscillation and corresponding acceleration of the airfoil, at $Re=145976$, Spring 1, Angle 3. Numbers at the left bottom corners of the images and the corresponding numbers on the acceleration graph indicate the instant when the image is taken..	57
Figure B3.2	: Vorticity formation around the airfoil for one period of oscillation and corresponding acceleration of the airfoil, at $Re=141981$, Spring 2, Angle 3. Numbers at the left bottom corners of the images and the corresponding numbers on the acceleration graph indicate the instant when the image is taken..	58
Figure B3.3	: Vorticity formation around the airfoil for one period of	

oscillation and corresponding acceleration of the airfoil, at $Re=144650$, Spring 3, Angle 3. Numbers at the left bottom corners of the images and the corresponding numbers on the acceleration graph indicate the instant when the image is taken.. 59

Figure B3.4 : Vorticity formation around the airfoil for one period of oscillation at $Re=75189$, Spring 1, Angle 2 and corresponding acceleration, velocity and the displacement of the airfoil..... 60



LIST OF SYMBOLS

$\mathbf{a_t}$: Tangential acceleration
α	: Angle of Attack (AOA)
\mathbf{c}	: Airfoil chord length
δ	: Logarithmic decrement
Δt	: Time difference between two pulses
\mathbf{f}	: Pitching frequency
\mathbf{Re}	: Reynolds Number
$\mathbf{T_d}$: Period of free underdamped vibration
$\mathbf{U_\infty}$: Free stream velocity
ω	: Vorticity
ω_d	: Damped natural frequency
ω_n	: Natural frequency
ω_r	: Reduced frequency
ω	: Circular Frequency
ζ	: Damping ratio

SELF-INDUCED PITCHING OSCILLATIONS OF AN AIRFOIL

SUMMARY

In this study, the focus is on the self-induced oscillations of a NACA 0012 airfoil. The relationship between the moments acting on the airfoil and the vortex formation in the near-wake of the airfoil is investigated via Digital Particle Image Velocimetry (DPIV) in conjunction with instantaneous acceleration measurements.

The airfoil is free to undergo pitching oscillations about the quarter chord location. Different freestream velocities, different springs to yield different stiffnesses for the structure and different initial conditions in terms of angle of attack before the airfoil is let to oscillate have been chosen to investigate the phenomena.

Experiments of this study have been performed in the 50 cm × 50 cm Low Subsonic Wind Tunnel (50×50 LSWT) in Trisonic Research Center at Istanbul Technical University. Different freestream velocities between 7.0 m/s – 17.0 m/s, corresponding to Reynolds numbers of $59-148 \times 10^3$ are used. The natural frequencies of the system are measured to be 57.12 Hz, 36.96 Hz, and 62.98 Hz. The reduced frequency, is between 0.26 - 0.49 for the investigated cases.

The initial goal of the study has been to obtain flow-induced oscillations of an airfoil in the velocity range supplied by the wind tunnel in use. Then, quantitative flow field measurements are refined around the oscillating airfoil. Acceleration measurements are adopted to get information on the moments acting on the airfoil while oscillating. Angular velocity and position of the airfoil are obtained for selected cases, related to the vorticity formation in the near-wake of the airfoil. The integration of the acceleration data has been also checked with the position of the airfoil obtained from PIV images.

The vortex formation patterns are correlated with the acceleration signal. It has been observed that the small modulations correspond to some intermediate shedding. Especially the shedding of the stall vortex is correlated with the local or absolute minimum before the absolute maximum on the acceleration signal. As the angular position of the airfoil could be determined via integration of acceleration, it is possible to state that the formation of the stall vortex starts just after the mean value when the angle of attack is increasing and the stall vortex is shed just after the mean value is attained when the angle of attack is decreasing.

BİR KANAT PROFİLİNDE AKIŞIN UYARDIĞI YUNUSLAMA SALINIMLARI

ÖZET

Bu çalışmanın odak noktası NACA 0012 kanat profilinde akışın uyardığı yunuslama salınımlarıdır. Kanat profiline etkiyen momentler ve yakın iz bölgesindeki vorteks oluşumu arasındaki ilişki, anlık ivme ölçümleri ile birlikte DPIV (dijital olarak parçacık izleyerek hız belirleme sistemi) kullanılarak incelenmiştir.

Kanat profili, hücum kenarından çeyrek veter boyu uzaklıktaki eksen çevresinde yunuslama salınımları yapmaya serbesttir. Konuyu incelemek için değişik serbest akım hızları, model için değişik sertlikler elde etmek üzere değişik yaylar ve çeşitli hücum açısı değerleri kullanılmıştır.

Deneyler İstanbul Teknik Üniversitesi, Trisyonik Araştırma Merkezi 50 cm × 50 cm Sesaltı Rüzgar Tüneli'nde yürütülmüştür. Deneylerin yapıldığı serbest akım hızları 7.0 m/s – 17.0 m/s aralığındadır. Bu değerlere karşılık gelen Reynolds sayıları $59 \cdot 10^3$ – $148 \cdot 10^3$ aralığındadır. Modelin doğal frekans değerleri, farklı konfigürasyonlar için 57.12 Hz, 36.96 Hz. ve 62.98 Hz. olarak ölçülmüştür. İncelenen durumlar için indirgenmiş frekans değerleri 0.26 - 0.49 aralığındadır.

Bu çalışmanın ilk hedefi, kullanılan rüzgar tünelinin sağlayabildiği akım hızlarında, kanat profilinin akışın uyardığı salınımlarının elde edilmesi olmuştur. Devamında, profil etrafında akım alanının niceliksel incelenmesine yönelik iyileştirme çalışmaları yapılmıştır. Profil salınım yaparken üzerine gelen momentleri belirlemeye yönelik olarak ivme ölçülmüştür. Seçilen bazı durumlar için açısal hız ve pozisyon değerleri, profil yakın iz bölgesindeki çevri oluşumu ile ilişkilendirilmiştir. İvme verilerinin integreasyonu, PIV görüntülerinden elde edilen konum bilgisi ile de doğrulanmıştır.

Vorteks oluşum yapıları ivme sinyalleri ile ilişkilendirilmiştir. Küçük ivme modülasyonlarının ara vorteks kopmasına sebep olduğu gözlenmiştir. Özellikle taşıma kaybı ile ilgili vorteks kopması durumlarında, ivme sinyalinin mutlak maksimum değerinden önce görülen bölgesel veya mutlak minimum değerlerinde olduğu gözlenmiştir. İvme sinyalinin integre edilmesi ile kanadın açısal konumunun belirlenebilmesi sonucunda, kanat konumu - taşıma kaybı ile ilgili vorteks oluşumu ve kopması arasındaki ilişkilere ulaşmak mümkün olmuştur. Buna göre, taşıma kaybı ile ilgili vorteks, kanat profilinin hücum açısı değeri artmakta iken ortalama açı değerine ulaşıldığında oluşmaya başlamaktadır. Taşıma kaybı ile ilgili vorteksin kopması ise hücum açısı değeri azalmakta iken ortalama açı değerine ulaşıldığında olmaktadır.

1 INTRODUCTION

Studies of unsteady-airfoil flows have been motivated mostly by efforts to avoid or reduce undesirable effects such as flutter, vibrations, buffeting, gust response and dynamic stall. Some attention has also been given to potentially beneficial effects of unsteadiness, such as propulsive efficiency of flapping motion, controlled periodic vortex generation, stall delay, and improving the performance of helicopter rotors, turbomachinery and wind turbines by controlling the unsteady forces in some optimum way. Both cases require predicting the magnitude and phase lag of the unsteady fluid-dynamic loads on lifting surfaces [1].

Determination of the forces on an oscillating airfoil is not an easy task. Force balance measurements can suffer from interference from structural resonances and static pressure distribution measurements can suffer from spatial resolution and sensor limitations [2]. However, non-intrusive experimental techniques in determining the unsteady velocity field around the structures and forces are promising [2-10].

In this study, the focus is on the self-induced oscillations of a NACA 0012 airfoil. The relationship between the moments acting on the airfoil and the vortex formation in the near-wake of the airfoil is investigated via Digital Particle Image Velocimetry (DPIV) in conjunction with instantaneous acceleration measurements.

The airfoil is free to undergo pitching oscillations about the quarter chord location. Different freestream velocities, different springs to yield different stiffnesses for the structure, and different initial conditions in terms of angle of attack before the airfoil is let to oscillate have been chosen to investigate the phenomena.

The initial goal of the study has been to obtain flow-induced oscillations of an airfoil in the velocity range supplied by the wind tunnel in use. Then, quantitative flow field measurements are refined around the oscillating airfoil. Acceleration measurements are adopted to get information on the moments acting on the airfoil while oscillating. On the other hand, although difficulties exist for the integration of the time history of

the acceleration, the calculated velocity and position data lead to the use of the equation of motion.

Although, instantaneous velocity and vorticity fields correlated with the acceleration allow insight into the physics of the phenomena, some attempts have been made to set the equation of motion. Angular velocity and position of the airfoil are obtained for selected cases, related to the vorticity formation in the near-wake of the airfoil. The integration of the acceleration data has been also checked with the position of the airfoil obtained from PIV images.

Another aspect of the current study is its experimental setup which allows illumination of the whole flow field, both the suction and pressure sides of the airfoil, and consists the major difference of the investigation when compared with others in the literature.

The insight gained in this study will provide basis for future work on the active and passive control of the vortex shedding over an airfoil. The results already constitute validation data for numerical analyses.

2 LITERATURE REVIEW

The rapid incidence variations of an airfoil and associated dynamic features were first recognized by Kramer in 1932 [11]. Until 1960's, the topic received little attention by the aerodynamicists. When the same phenomena has been encountered on helicopter blades, oscillating airfoil became one of the most studied topics.

In 1972, McCroskey and Fisher [12] showed that it is possible to simulate the basic effects of a stalled rotor blade in a realistic way by a 2-D sinusoidally pitching airfoil. In the meantime, it was noticed that sinusoidal pitching motions are close to the incidence variations experienced by real rotor blades. Therefore, investigations have been especially focused on sinusoidal pitching motions.

In 1977, Carr, McAlister and McCroskey [13] stated the relation between the main features observed on the lift and the pitching moment curves. They also observed the formation, development and subsequent shedding of organized vortex structures on the airfoil. Since then, experimental studies have been mainly conducted by using flow visualization techniques, pressure measurements and velocity measurements by hot wire technique.

In 1983, De Ruyck and Hirsch [14] obtained the detailed velocity and Reynolds stress profiles by the hot wire technique at different downstream positions in the wake of a sinusoidally pitching NACA 0012 airfoil. The instantaneous incidences have been varied from zero to just above the static stall limit for Reynolds number 3×10^5 . They have observed the trailing-edge stall as the static incidence reaches 14° .

In 1988 Kim and Park [15] visualized the chronological flow patterns around an airfoil, forced to oscillate in pitch, by using the smoke wire technique. They showed that the instantaneous angle of attack at which the separation takes place, depends on the reduced frequency ω_r , and that for flows with larger ω_r , the separation occurs at a larger phase angle wt .

In 1990, Park et al. [16] studied the unsteady near wakes behind an oscillating NACA 0012 airfoil in pitch about the quarter chord location. They obtained the ensemble-averaged mean velocity and turbulence intensity profiles and observed that the mean velocity profile at each downstream station exhibits a phase lag relative to the periodic motion of the airfoil and the phase lag was found to increase with downstream distance.

In 1990, Leishman [17] examined the static and dynamic stall characteristics of NACA 23012 airfoil at Reynolds number of 15×10^5 by using miniature pressure transducers and hot film gauges. By numerically integrating the pressure distribution, he obtained the lift and the pitching moments. As a conclusion, he found that a positive pitch rate and thus increased reduced frequency provides a beneficial effect and helps keep the boundary layer attached to very much higher angles of attack over those, which could be obtained statically.

In 1999, Lee et al. [18] determined the instantaneous locations of unsteady boundary layer transition, separation and reattachment on an NACA 0012 airfoil by using multiple hot film sensors. They found the boundary-layer transition and separation points to be delayed with increasing reduced frequency during pitch up and decreasing reduced frequency during pitch down.

With the progress in optics, electronics, lasers and signal processing, non-intrusive techniques such as Laser Doppler Anemometry (LDA) and Particle Image Velocimetry (PIV) became widely used techniques in oscillating airfoil studies. In 1994, Shih and Ho [19] used a stationary 2-D NACA 0012 airfoil placed at the static stall angle of 12 degrees in a vertical water tunnel to identify the evolving vorticity field of the airfoil. They used LDA to measure velocity, load cells to measure aerodynamic forces and a laser to visualize the flow field. They presented that the intricate variation of aerodynamic properties can be understood through the basic vorticity balance concept and the time scales of the flow field. They also showed that, for the unsteady attached flow, the reduced frequency has no physical meaning due to the lack of the intrinsic flow time constant. Therefore, the unsteady aerodynamic properties depend on the reduced frequency only if the flow is separated.

To study the mechanisms involved in an unsteady flow, it would be advantageous to have instantaneous velocity field data. For this reason, a global method such as PIV technique is best suited to achieve the goal rather than a pointwise measurement technique such as LDA. Shih et al. (1992) [20] are the pioneers to use PIV. They investigated the unsteady flow past a NACA 0012 airfoil in pitching-up motion in water towing tank using the Particle Image Displacement Velocimetry (PIDV). They proved the ability of the PIDV technique to provide instantaneous velocity and vorticity fields of high spatial resolution and accuracy for such complex flow fields. They also presented the leading-edge flow separation to occur for $\alpha > 20^\circ$. They visualized that the leading edge vortex dominating the flow moves downstream and grows to a size that is comparable with the airfoil chord. They also observed the evolution of a counter-rotating vortex formed from the trailing edge when the leading edge vortex comes sufficiently close to it.

In 1995, using PIV in a low speed wind tunnel, Raffel et al. [21] investigated the unsteady flow field above a NACA 0012 airfoil pitching under deep dynamic stall conditions. These experiments were conducted in wind tunnel rather than the water tunnel to obtain higher Reynolds numbers, which represents more accurately the dynamic stall phenomena for rotor blades. They obtained the velocity fields with a high spatial resolution.

In 1996, Wernert [22] et al. investigated the dynamic stall process on a pitching NACA 0012 airfoil experimentally by PIV, laser-sheet visualizations and numerically by a code based on Navier-Stokes equations. They have presented the evolution of the dynamic stall process as attached flow, development of dynamic stall vortex, post stall vortex shedding and reattachment processes both experimentally and numerically. They also showed the aperiodicity of the flow phenomenon when massive flow separation occurs.

In 1997, Wernert et al. [23] took PIV data in 1° -incidence steps during the entire oscillation cycles to obtain the complete description of the phenomena. They also used LDA to compare it with PIV for oscillating airfoils. They showed that the flow becomes completely non-reproducible within a few milliseconds between incidences of 24 and 25 degrees upward motion which can be considered as typical of a chaotic process.

In 1997, Oshima and Ramaprian [24] presented the instantaneous velocity measurements on the suction side of a NACA 0015 airfoil pitching at a constant angular velocity about its quarter-chord span wise axis. They studied the formation, evolution and the shedding of the LEV (leading edge vortex) and DSV (dynamic stall vortex) via PIV.

As it became evident that the loading on an airfoil is directly related with the velocity distribution and its derivatives [3,4], calculation of the forces and moments on the airfoil from these experimentally obtained quantities became one of the major research topics. Although the studies have been concentrated in the force prediction on two-dimensional circular cylinders, rigid, oscillating or in transitional motion [5-9], airfoil or flat plate investigations are also undertaken [2,10].

In 1994, Panda and Zaman [2] studied the sinusoidal pitching of an airfoil at Reynolds numbers of $22\text{--}44 \times 10^3$ to relate the flow field with the loading. They observed that the sum of the absolute values of all vorticity convected into the wake over a cycle is nearly constant and is independent of the reduced frequency and amplitude of oscillation. They estimated the time varying component of the lift from the shed vorticity flux. Depending on the comparison of the lift hysteresis loops with corresponding vorticity fields, they showed that the major features of the lift variations are directly linked to the evolution of the large-scale vortical structures and the phase delay phenomenon.

3 EXPERIMENTAL SETUP

3.1 Wind Tunnel

Experiments of this study have been performed in the 50 cm \times 50 cm Low Subsonic Wind Tunnel (50 \times 50 LSWT) in Trisonic Research Center at Istanbul Technical University. The tunnel has a cross sectional area of 500mm \times 500mm at the entrance of the test section and 540 mm \times 540 mm at the exit to establish a uniform flow in the desired cross sectional area without the influence of the boundary layer (Figure 3.1). The sidewalls of the tunnel are constructed by transparent Plexiglas, allowing the use of laser based techniques such as PIV and LDA. It is also equipped with a ventilation unit to take out the seeding materials out of the medium (Figure 3.2). The freestream turbulence level of the tunnel is 0.3% according to previous studies [25] and it is capable of supplying freestream velocities in the range of 3 m/s to 30 m/s.

3.1.1 Flow speed measurement

A fan, driven by a Femsan 7.5 kW DC motor, operates 50 \times 50 LSWT and a Siemens Simoreg D485/30 type control unit controls the motor. Freestream velocities in this study are determined using a Pitot static tube that is connected to a Setra absolute pressure transducer with a measurement range of ± 25.4 mm-H₂O. Pitot static tube is carefully placed downstream of the airfoil, close to the upper wall, so that it does not influence the boundary layer. Simultaneous freestream velocity measurements are accomplished during the preliminary experiments by using Pitot static tube and PIV; results compared for a common point are in good agreement with each other. Measurement procedure and results will be presented in detail in § 4.1. The investigation is continued only with Pitot static tube measurements for freestream velocity determination.

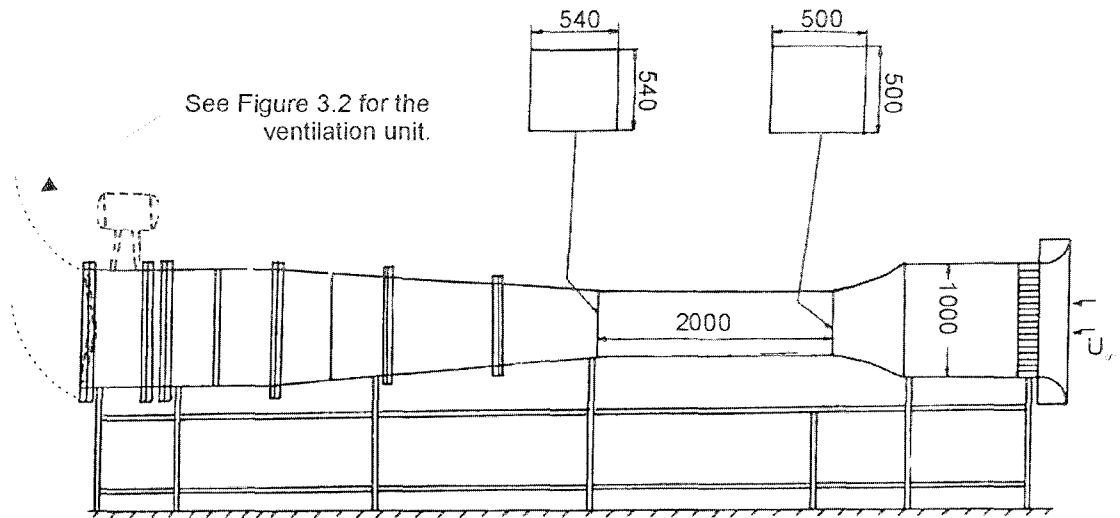


Figure 3.1 Side view of the 50x50 LSWT

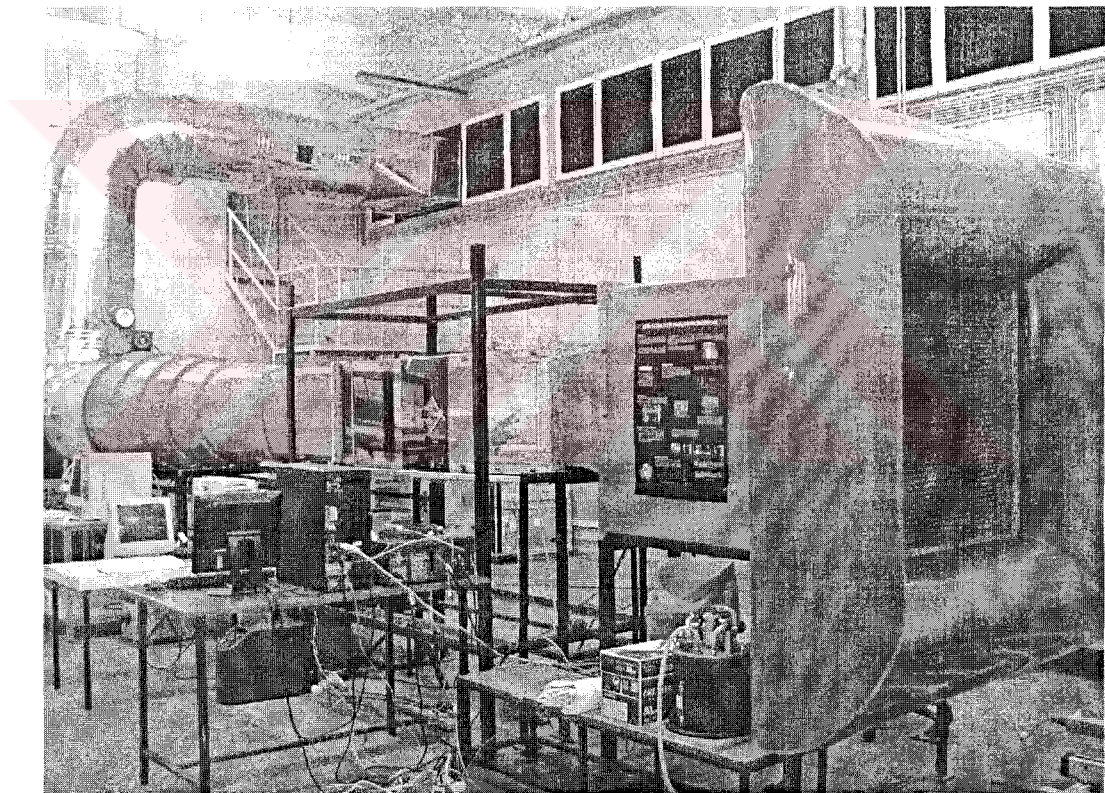


Figure 3.2 View of the 50x50 LSWT with the ventilation unit

Freestream velocity is one of the major parameters affecting the reduced frequency. In this study, the experiments are conducted at freestream velocities ranging from 7 m/s to 17 m/s. In the context of the investigation, three different speeds are used to establish the variation.

3.2 Airfoil and Mounting

The experiments have been performed using a NACA 0012 airfoil with a chord length of $c=120$ mm and a span of 518 mm. The sidewalls of the tunnel are used as endplates, therefore the flow is assumed to be two-dimensional.

The airfoil is manufactured as 2 pieces, each with a span of 254 mm, from blue Styrofoam. A steel rod with a diameter of 4 mm passes through the axis, located at the quarter chord distance away from the leading edge. The two airfoil pieces are fixed onto this rod with 10 mm spacing in between, using epoxy to prevent any relative motion with respect to each other. The coating of the airfoil is made of a self-adhesive transparent paper to establish a smooth surface and to allow illumination of both the pressure and suction sides of the airfoil at its mid-section. Two ball bearings with an inner diameter of 4 mm are mounted on Plexiglas sidewalls of the wind tunnel and hold the rod of the airfoil. Detailed pictures can be seen in Figure 3.3.

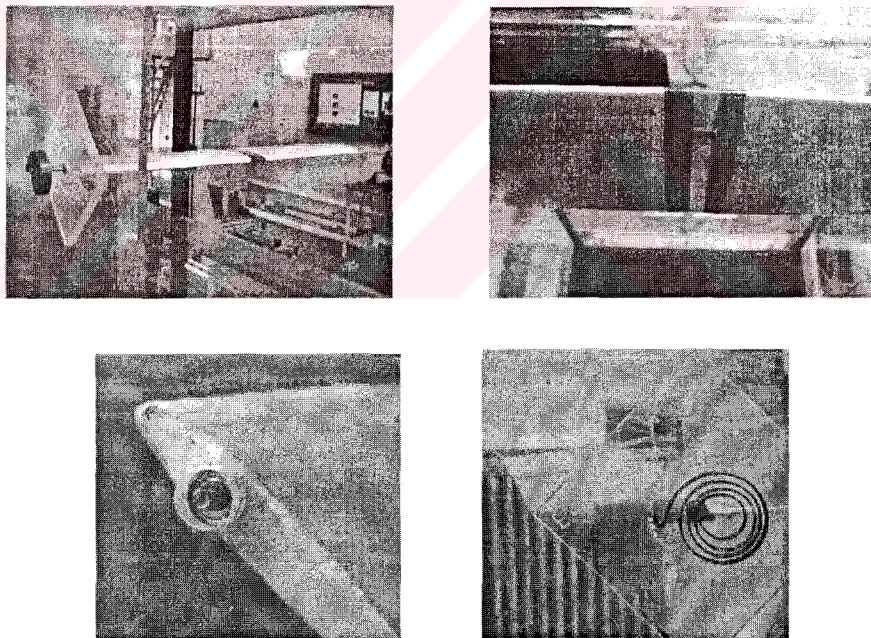


Figure 3.3 Pictures showing airfoil, its mounting and angle of attack mechanism from different angles of view

A Plexiglas plate is manufactured with a series of holes on it, one at the center for the rod and the others concentrically spaced to position the airfoil at different angles of attack. One of the ends of a helical spring is mounted to the rod outside the tunnel and the other end to a pin inserted in one of the holes on the Plexiglas plate. Three

different springs are used to obtain different natural frequencies for the system including airfoil, shaft and spring (Figure 3.4).

The natural frequencies of the system are measured to be 57.12 Hz, 36.96 Hz, and 62.98 Hz. The schematic of the experimental setup is shown in Figure 3.5.

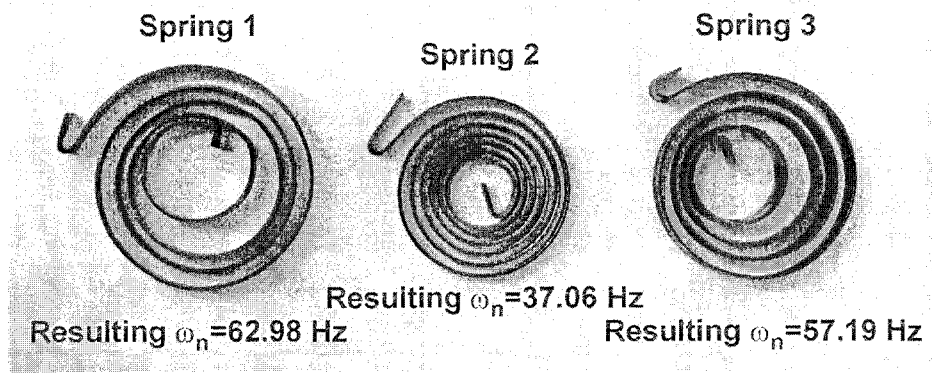


Figure 3.4 Springs used in the study

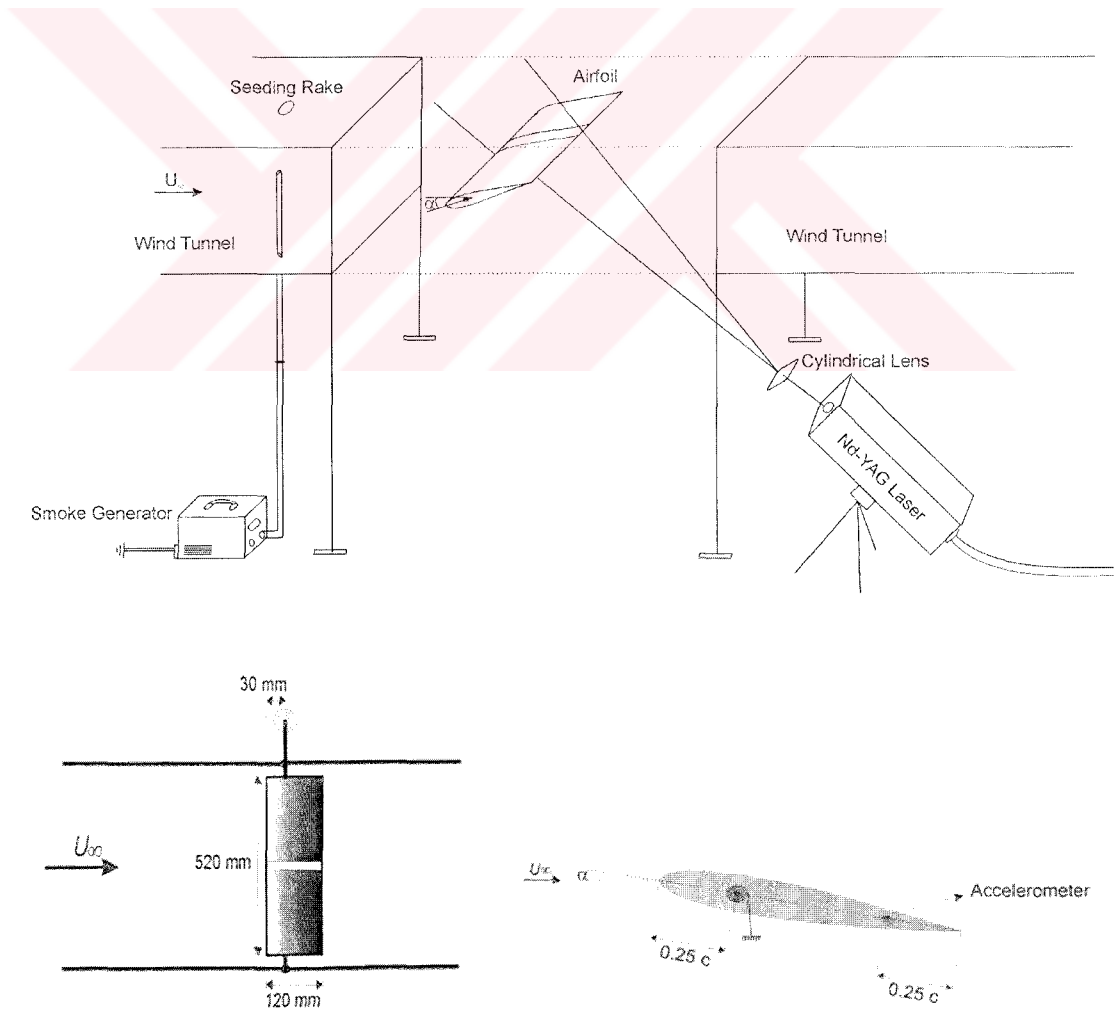


Figure 3.5 Experimental Setup of the study

3.3 Accelerometer

A PCB 352C22 model miniature, ceramic shear ICP accelerometer and a 4 channel PCB 442A04 model signal conditioner is used to determine the instantaneous accelerations of the airfoil. The accelerometer with 11.4mm×6.4mm dimensions and a mass of 0.5 g is inserted in the Styrofoam of the airfoil, quarter chord distant from tip, in a spanwise location close to the wind tunnel wall. Its sensitivity is 9.39 mV/g, frequency range 1 to 100,000 Hz. The broadband resolution of the accelerometer is 0.002 g rms and its measurement range is ± 500 g. Representative drawing of accelerometer mounting, pictures of the accelerometer and the conditioner can be seen in Figure 3.6.

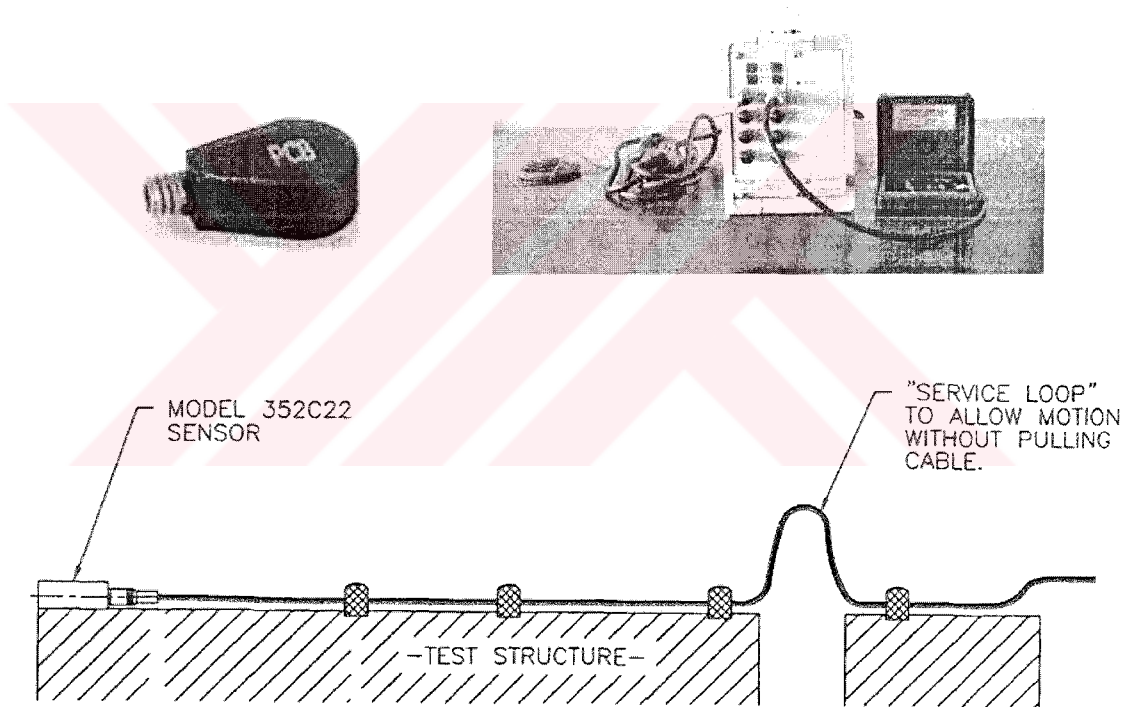


Figure 3.6 PCB Accelerometer, conditioner and mounting

3.4 Laser and Camera

Quantitative flow images are captured and processed by Digital Particle Image Velocimetry (DPIV) system. A Redlake MegaPlus ES 1.0 8 bit digital camera with 1008H × 1016V pixel resolution is used for image acquisition. The double frame rate

of the camera is 15 Hz. The speed of the camera does not allow taking more than one vector field per oscillation cycle.

The flow is illuminated by a New Wave Solo-PIV 120 Nd:Yag laser with two cavities each providing 15 Hz repetition rate. The maximum output energy is 120 mJ per pulse at 532 nm wavelength with pulse duration of 3-5 ns. Two cylindrical lenses are used to generate a laser sheet with the desired dimensions at the investigation region. However, the camera captures a 254.1mm \times 256.1mm cross sectional flow field. A Dantec 2100 system hub, with a LIFO Buffer capacity of 1.5 GByte is provided the physical communication links and synchronization between the computer, laser and the camera. Pictures of the components of PIV system are given in Figure 3.7.

3.5 Seeding

The flow is seeded by a SPT Smoke Generator that burns paraffin oil (Shell Ondina Oil Type 15). Different seeding approaches and equipments were used and as a conclusion, a rake, placed upstream of the airfoil is found to be the most effective one.

The rake, manufactured from a 6 mm aluminum pipe with 40 holes on it, is vertically placed inside the tunnel, at the mid section, 480 mm in upstream of the airfoil corresponding to 80 pipe diameters. This value exceeds 6.5D, the minimum distance stated by [26] to regain uniform flow conditions downstream of a circular cylinder.

The smoke generator is mounted to the rake and paraffin oil is used as the seeding material. The mean particle size is 1.5 μm within the range of 1-4 μm and the refractive index of 1.468.

3.6 Data Acquisition

In order to correlate the acceleration measurement results and the flow field images, simultaneously acquired acceleration and PIV data are synchronized using the laser pulse signal.

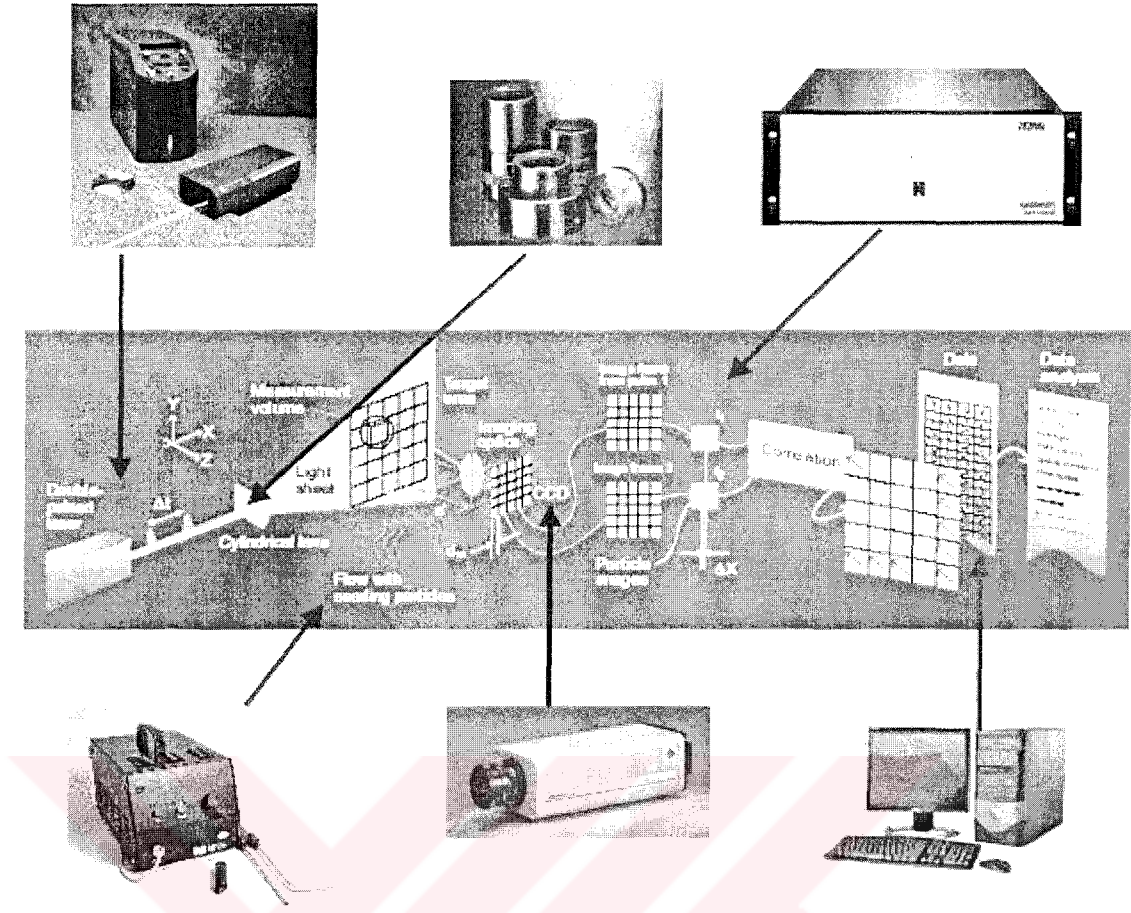


Figure 3.7 Schematic of PIV processes and components used in the study

A 5.0 V TTL synchronization signal sent by the laser controller for each pulse is acquired with the acceleration signal. The duration of the signal is almost $110\mu\text{s}$ and the laser is pulsed with 60 ns latency with the synchronization signal. The time delay between the two pulses is determined as $90\mu\text{s}$ for the experiments to meet the dynamic range of the flow. The time difference between the recordings, consisting of following 2 pulses, is 66.6 ms depending on the maximum frame rate of the camera. Figure 3.8 shows the time-diagram. A data acquisition card, NI PCI-6014, with 300 kHz sampling rate is used along with a LabVIEW VI (Virtual Instrument).

Different freestream velocities between 7.0 m/s – 17.0 m/s, corresponding to Reynolds numbers of $59\text{-}148 \times 10^3$ are used. For each freestream velocity, different angle of attack values are defined by changing the position of the pin on the plate. Instantaneous positions of the airfoil are determined by graphical processing of the PIV images. The analysis of the results yields the reduced frequency, which is given by Equation (3.1), to be between 0.26 - 0.49 for the investigated cases.

$$\omega_r = \frac{2\pi f c}{2U_\infty} \quad (3.1)$$

In equation 3.1, f is the oscillation frequency in Hz, c chord of the airfoil and U_∞ represents the freestream velocity.

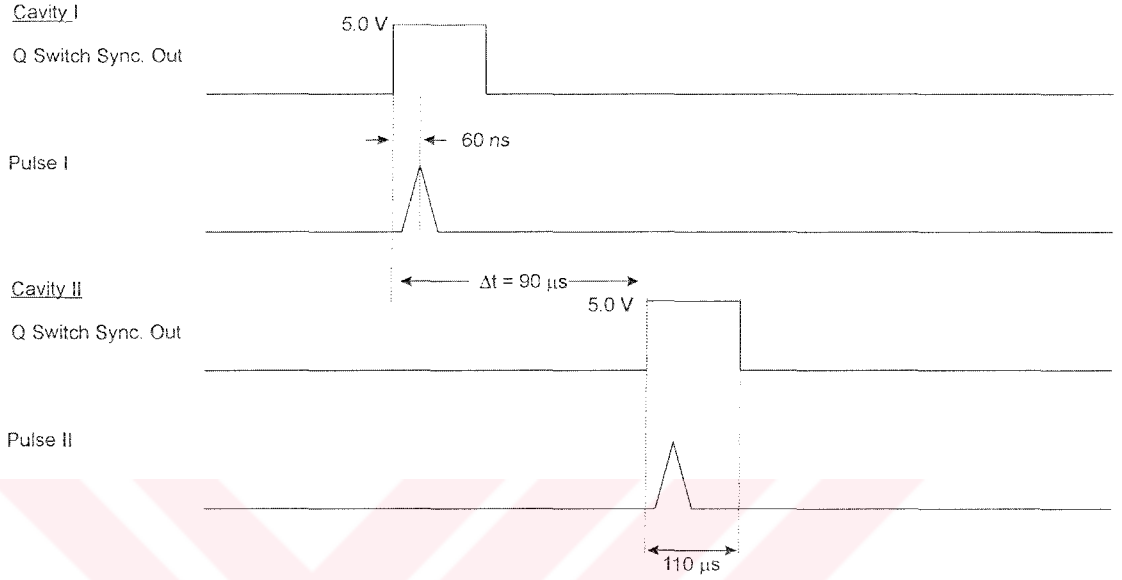


Figure 3.8 Time diagram of PIV system

Synchronization signal duration of the laser pulse is 110 μs and the first harmonic of the pitching motion of the airfoil is in the order of 10 Hz. In order to meet the Nyquist criterion for both of the signals, the data is acquired at 20 kHz. Although sampling frequency of 100 Hz. is determined to be good enough for acceleration measurements, it is set to 20 kHz according to the restriction for the duration of the laser pulse synchronization signal. Then a 2nd order Butterworth band pass digital filter is used to filter the acceleration signal with a low cutoff frequency of 3 Hz and high cutoff frequency of 50 Hz in order to remove noise from the data.

3.7 Post Process

Post processing of the PIV image pairs were done in a two step manner: in the initial step, Dantec FlowManager Software is used for data acquisition and initial processing of the raw image pairs. FlowManager is the control software of the PIV system, at the same time, it has routines for the post processing of the images and a MatLab-link for user defined processes. As a first step, the image pairs are processed

with a MatLab-script that uses top-hat filtering to remove the background from the images. Top-hat filtering script removes partly the shadows that exist at the leading and trailing edge of the airfoil due to the transparent coating and at the shaft location; it essentially increase the contrast of the image and make the seeding particles detectable. One of the raw images and its filtered version can be seen in Figure 3.9. Filtered image pairs are cross-correlated to get the raw velocity fields. The cross correlation is performed on 64 by 64 pixels interrogation windows that correspond to a resolution of $16\text{mm} \times 16\text{mm}$ in the physical plane of laser sheet. The interrogation windows in two images are 50% overlapped in freestream direction and in the normal direction to the freestream. Differences between the velocity fields obtained from the raw image and the filtered image can be seen in Figure 3.10. Necessity for such a filtering is clearly visible from the results of these two images.

Raw velocity fields contain some erroneous vectors known as “bad vectors” because of the shadows and objects in the flowfield, un-seeded or over-seeded regions, etc. Therefore, an initial vector cleaning, namely Range Validation, is used in FlowManager. The Range Validation routine depends on minimum and maximum velocity components allowed in the flowfield to exist, for the validation of the vectors. For most of the cases, this routine is not enough to clean all incorrect vectors. Although several routines are available in Dantec FlowManager, range validated vector fields are exported to be processed by non-commercial programs due to format problems and lack of flexibility to further process the data and present the results in FlowManager. Range validated velocity field can be seen at the left in Figure 3.11. Incorrect vectors that can not be cleaned by the range validation can be seen in black circles at the right in Figure 3.11.

For the latter analysis, non-commercial programs V3 and NFILVB are employed to visualize and manually clean the bad vectors, to fill the areas of missing vectors, and to compute the vorticity distribution. The range validated vector fields are viewed using V3 which allows user to determine and remove incorrect or bad vectors from the interrogation (Figure 3.12). On the other hand, NFILVB employs a bilinear least-square fit technique on the surrounding vectors to interpolate the areas where incorrect vectors have been removed. The resulting velocity field is also smoothed by this program using a Gaussian-weighted technique based on Landreth and Adrian

(1989) [27] (Figure 3.12). A suggested smoothing parameter of 1.3 is used for the results of this study. Images are also exported as *.tiff files to determine the instantaneous angle of attack (AOA) of the airfoil using image processing softwares. NFILVB uses the resulting boundary information for the airfoil to set the proper conditions of interpolation.

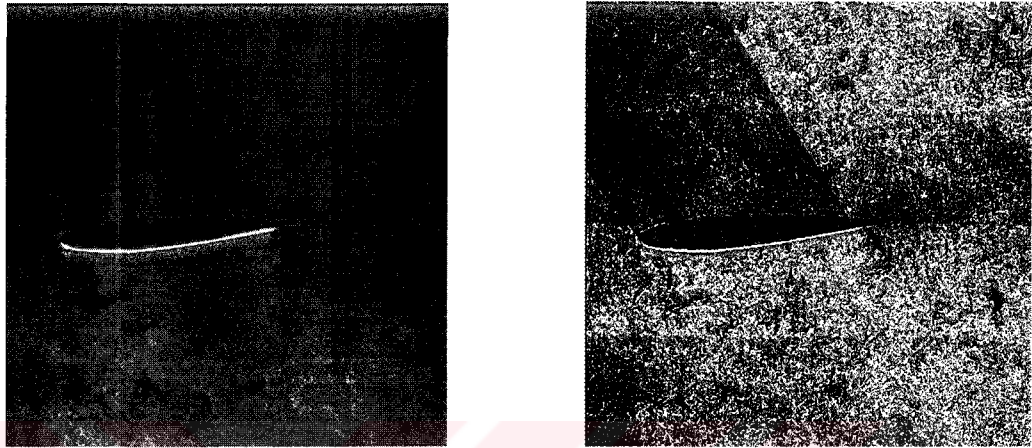


Figure 3.9 Raw PIV image and the top-hat filtered version of the same image

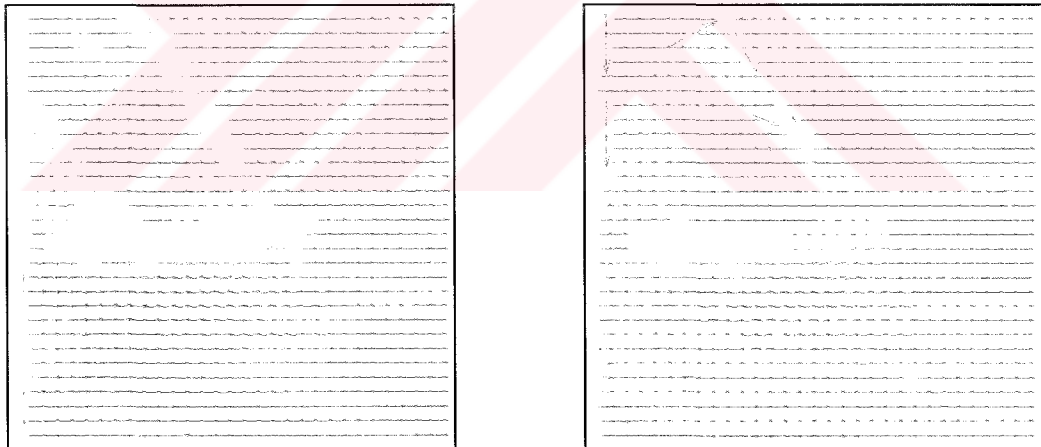


Figure 3.10 Velocity fields obtained from the raw image and the filtered image

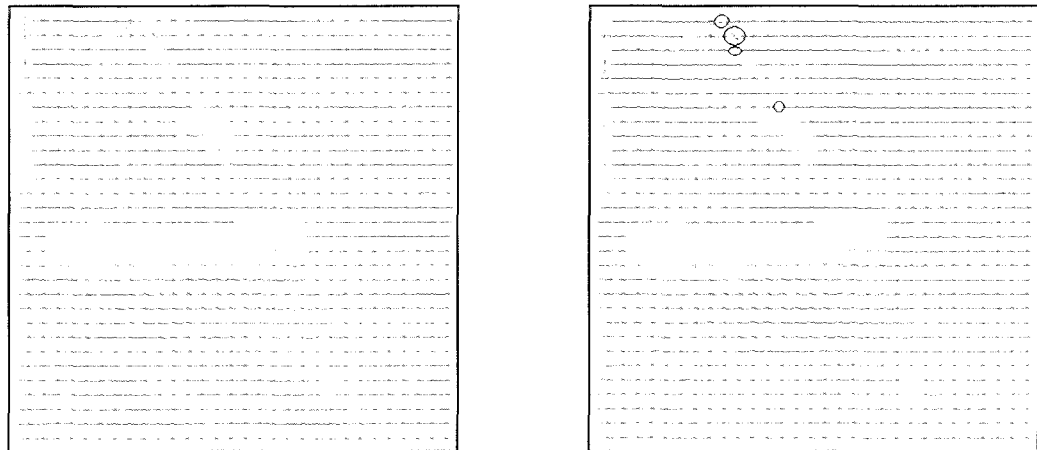


Figure 3.11 Range validated velocity field and the remaining bad vectors

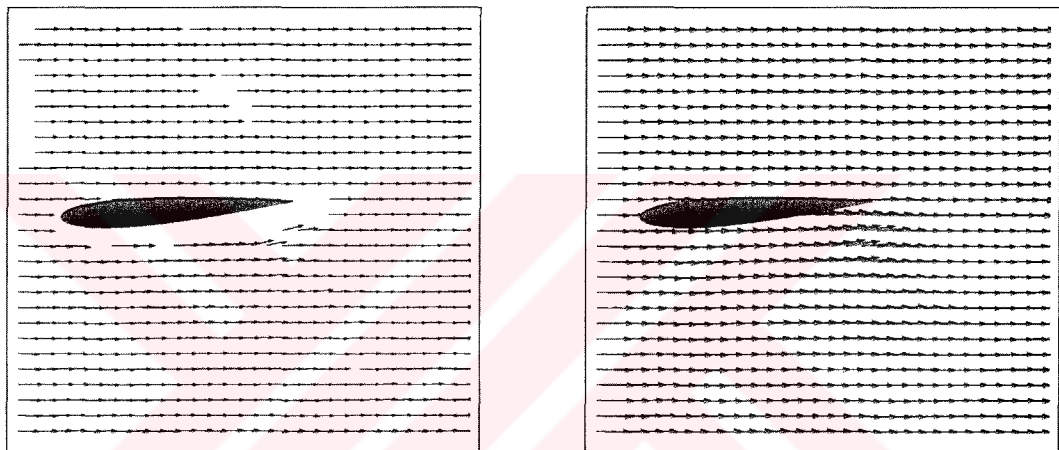


Figure 3.12 Cleaned velocity field by V3 and the result after the NFILVB process

4 RESULTS

Results are given in three subsections. In the first section, the uniformity of the freestream in the test section is investigated. In the second section, structural properties of the system are presented based on accelerometer measurements and related calculations. Finally, self-induced pitching oscillations of the airfoil is discussed in terms of the results of PIV and correlated with acceleration data.

4.1 Wind Tunnel Performance

Preliminary experiments are conducted to determine the flow quality of the wind tunnel. Pitot static tube and PIV measurements are simultaneously performed to validate reliability of the velocity determination via Pitot static tube in conjunction with pressure transducers and to determine the uniformity of the freestream.

4.1.1 Pressure transducer validation

A Pitot static tube is placed inside the flow for the freestream velocity measurements. Position of the Pitot static tube relative to the tunnel can be seen in Figure 4.1. Static and total pressure output of the Pitot static tube is connected to the Setra Absolute Pressure Transducer, placed outside the wind tunnel.

For the validation of the data obtained by the pressure transducers, two identical transducers are used. Static and total pressure outputs of the Pitot static tube are connected to 2 channels by using T adapters for each output. Then the channels are connected to the pressure transducers. Using an in-house VI written in LabVIEW, two-channel data is simultaneously acquired from the transducers.

The tunnel speed is adjustable by a knob on the control unit and the velocity range of the wind tunnel, which is 3 to 30 m/s, corresponds to knob position values in the

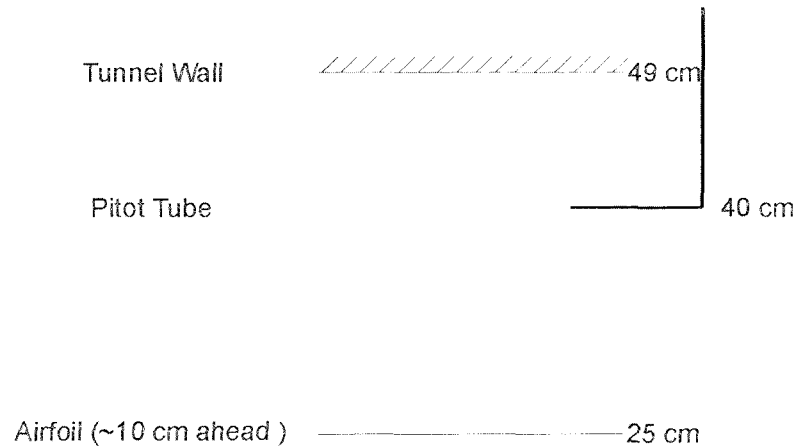


Figure 4.1 Positioning of the Pitot static tube

range of 0 - 7. Taking into consideration the physical condition of the wind tunnel and the necessities of the study, test parameter is chosen to vary from 1.0 to 4.5 with 0.5 step values. Sampling frequency is set to be 100 Hz and the signals are recorded for a 60 s period of time. Measured dynamic pressure values are converted to velocity (m/s) via Bernoulli's equation. Average velocity values of measurements are given for each transducer in Table 4.1. Also, standard deviations are given for each measurement, obtained from the set of instantaneous measurement values. As can be seen from the table, maximum difference between the measurements performed by two transducers is 0.12 m/s, which does not exceed 0.7% of the mean velocity determined by the two transducers. Standard deviations are found to be a bit higher for the knob values lower than 2.0; corresponding to 8.5 m/s, which is chosen to be the lower limit for the experiments.

To see the stability of the freestream velocity, dynamic pressure measurements are taken with two transducers with a sampling frequency of 10 Hz for a period of 1500 seconds. This time, knob values of 1.5, 3.0 and 4.5 are chosen for the investigation. The average flow velocities and standard deviations are given in Table 4.2

If two aforementioned tables are compared, it can be seen that the standard deviation remains at the same order and the average velocity values are in agreement. This shows that the wind tunnel speed is stable for a time period of 25 minutes, which is long enough for a set of experiments. Slight variations of velocity for the same knob position of the controller at different runs are accounted for by measurement of velocity before each experiment.

According to the results, second pressure transducer employed in the experiments as it always gives a lower standard deviation value compared to the first one.

Table 4.1 Comparison of the results obtained by the transducers

Knob Pos.	Transducer 1		Transducer 2	
	Avg. Vel. (m/s)	Std. Dev.	Avg. Vel. (m/s)	Std. Dev.
1.0	4.22	0.925	4.27	0.705
1.5	6.45	0.712	6.55	0.482
2.0	8.45	0.640	8.57	0.381
2.5	10.71	0.466	10.81	0.286
3.0	12.72	0.396	12.83	0.261
3.5	14.76	0.370	14.85	0.252
4.0	16.82	0.342	16.94	0.246
4.5	18.90	0.352	19.02	0.251

Table 4.2 Stability data of the freestream velocity

Knob Pos.	Transducer 1		Transducer 2	
	Avg. Vel.	Std. Dev.	Avg. Vel.	Std. Dev.
1.5	6.23	0.799	6.44	0.523
3.0	12.72	0.431	12.85	0.276
4.5	18.73	0.342	18.85	0.251

4.1.2 Flow speed measurement via PIV

As a part of determining the uniformity of the freestream velocity, PIV measurements are performed for empty test section at a close location where the airfoil is mounted. The laser is positioned to illuminate the field upstream of the Pitot static tube that is connected to the pressure transducer. Figure 4.2 shows position of the flow field captured by the camera and the relative position of the Pitot static tube.

At this stage of the study, the flow field (127.1mm × 128.1mm) is captured and the images are cross-correlated with 64 by 64 pixels interrogation windows to get the velocity fields. As a result of using 64 by 64 pixels for cross correlation, the velocity field contains 30 by 30 vectors. The schematic for the arrangement of the vectors and a sample velocity field are shown in Figure 4.3. According to the position of the Pitot

static tube relative to the velocity field acquired by the PIV, the vectors in the 30th column and 8th (shown in Figure 4.3 with vector 30×8) are expected to match with the Pitot static tube results.

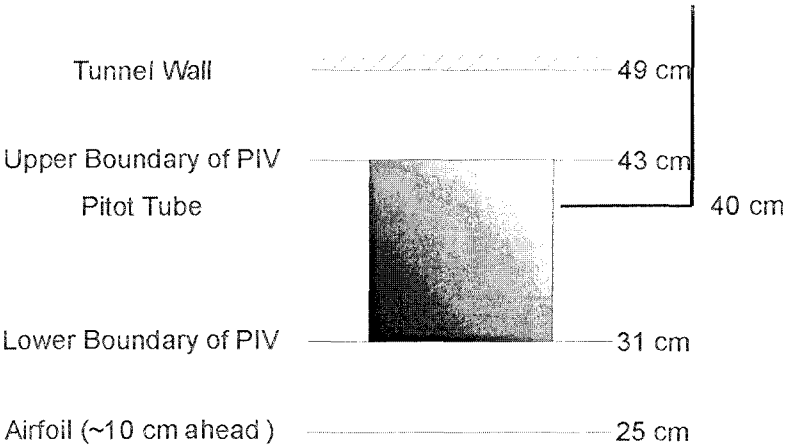


Figure 4.2 Positions of the Pitot static tube and captured flow field relative to each other

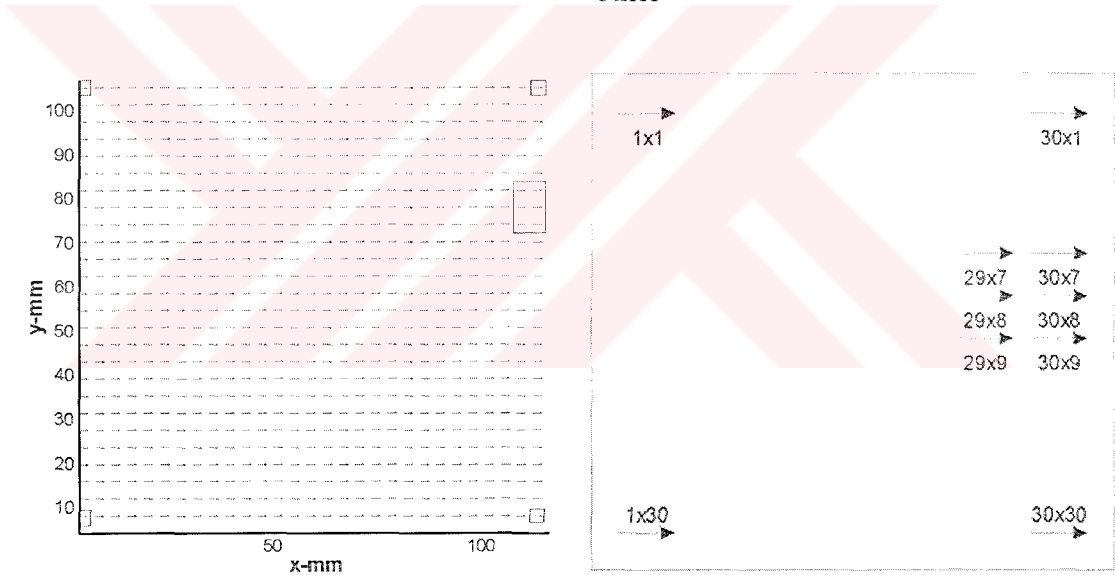


Figure 4.3 A sample velocity field and indexes of the vectors in the vector field

PIV measurements and Pitot static tube measurements are conducted simultaneously. For the PIV measurements, 100 image pairs are taken and processed to get the velocity fields. Then for each flow speed, the average velocity field is calculated. The standard deviation is also calculated for each vector position. Average velocity values and standard deviations of six vectors in the close neighborhood of the Pitot static tube are given for 8 knob positions in Table 4.3. Positions of these 6 vectors can be seen in Figure 4.3.

Average velocities and standard deviations for the simultaneous Pitot static tube measurements are given in Table 4.4.

Table 4.3 Velocity vectors obtained by PIV

Knob Values		1.0		1.5		2.0		2.5	
	Vector	Col 29	Col 30	Col 29	Col 30	Col 29	Col 30	Col 29	Col 30
Mean	Row 7	4.55	4.54	6.32	6.31	8.54	8.52	10.17	10.14
St. Dev.		0.145	0.156	0.238	0.241	0.214	0.211	0.353	0.360
Mean	Row 8	4.55	4.54	6.30	6.29	8.53	8.52	10.14	10.11
St. Dev.		0.146	0.160	0.218	0.225	0.211	0.214	0.350	0.354
Mean	Row 9	4.56	4.55	6.28	6.27	8.53	8.51	10.12	10.10
St. Dev.		0.133	0.143	0.195	0.206	0.214	0.225	0.345	0.348

Knob Values		3.0		3.5		4.0		4.5	
	Vector	Col 29	Col 30	Col 29	Col 30	Col 29	Col 30	Col 29	Col 30
Mean	Row 7	12.40	12.35	14.50	14.42	16.43	16.38	18.43	18.39
St. Dev.		0.423	0.487	0.791	1.141	0.699	0.924	0.531	0.531
Mean	Row 8	12.38	12.33	14.45	14.36	16.39	16.36	18.37	18.33
St. Dev.		0.472	0.580	0.842	1.218	0.568	0.662	0.592	0.646
Mean	Row 9	12.36	12.32	14.47	14.39	16.36	16.34	18.32	18.28
St. Dev.		0.468	0.578	0.700	0.964	0.513	0.534	0.598	0.646

Table 4.4 Velocity values obtained by Pitot static tube measurements

Knob Values	1.0	1.5	2.0	2.5
Mean	4.30	6.20	8.50	10.20
St. Dev.	0.852	0.785	0.628	0.532
Knob Values	3.0	3.5	4.0	4.5
Mean	12.40	14.70	16.40	18.4
St. Dev.	0.454	0.421	0.393	0.409

Velocity values of the vector 30×8 are highlighted in Table 4.3 for different knob positions. Pitot static tube measurement results for the same knob positions are also highlighted in Table 4.3 for the comparison. Corresponding values are found to be in good agreement except for the knob position 3.5. The standard deviation of the PIV results is very high for this knob position compared to the other cases. Later examination of the results for this case revealed low PIV image quality, high concentration of incorrect and interpolated vectors for this vector position in some of the averaged vector fields.

Pitot static tube is used in the oscillating airfoil case to precisely determine the freestream velocity to be used in the reduced frequency calculation. The experiments are conducted at the knob values of 2, 3 and 4 corresponding to freestream velocities of 8.5 m/s, 12.4 m/s and 16.4 m/s. The selection of these velocities is based on the preliminary experiments, which revealed different oscillation characteristics.

4.2 Structural Properties of the System

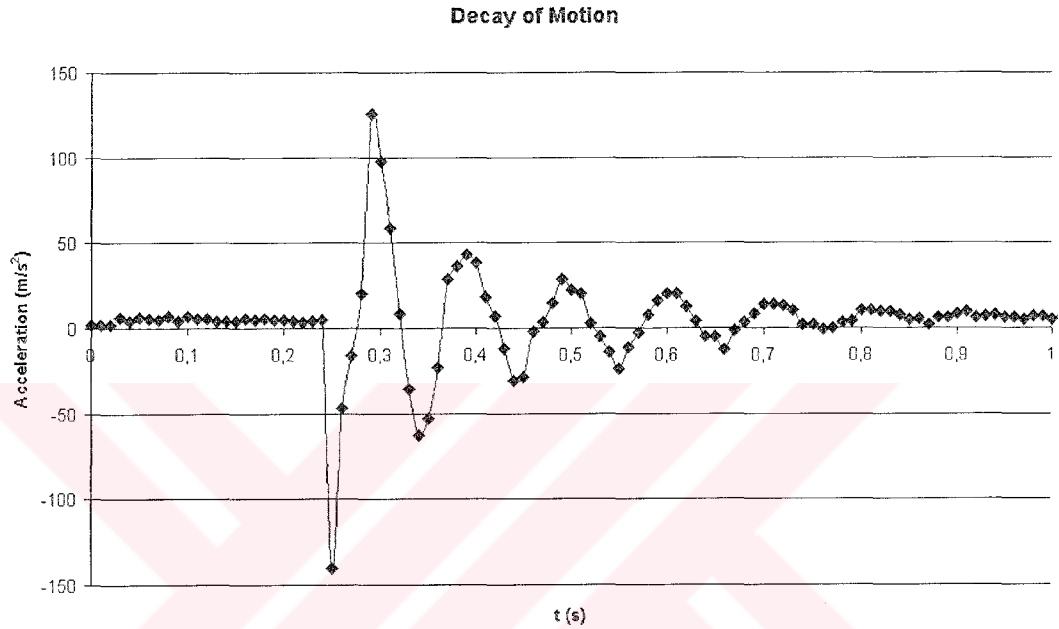
The total weight of the system which consists of the airfoil, its coating and the shaft is 82 grams. To obtain self-induced oscillations, the airfoil system is planned to be manufactured from materials as light as possible. Therefore, blue Styrofoam is used as the material of the airfoil and the shaft diameter is chosen as thin as possible without causing any loss in the rigidity of the system.

In the preliminary experiments, pitching frequencies of the airfoil are measured and found to vary in the range of 8 Hz to 13 Hz. On the other hand, the double frame rate of the PIV camera is 15 Hz. To reduce the oscillation frequencies, and therefore to acquire enough vector fields to represent a cycle of airfoil oscillation, additional masses are added to the end of the shaft. Although the oscillation frequencies are successfully reduced to almost 6 Hz, the amplitude of oscillations is also decreased a lot preventing to follow flow-structure interactions in motion.

Natural frequencies of the system are determined using a simple damping test in still air. Instantaneous impulses are given to the airfoil and the decay of the motion is recorded in terms of the acceleration signal. This process is repeated 40 times for each spring-airfoil system and the average values are used to calculate the natural frequencies. The angle of attack of the airfoil is also changed to see if its initial value before oscillation starts affects the natural frequency. In the calculations, effect of the position of the airfoil on the natural frequency is determined to be less than 1% of the calculated natural frequency. The formulas given in Appendix A are used for the calculations. Decay of the motion of the airfoil for a sample case is presented in Figure 4.4. Natural frequencies and other parameters are given for each spring-airfoil system in Table 4.5.

Table 4.5 Structural parameters of the airfoil-spring systems

	Spring 1	Spring 2	Spring 3
T_d (s)	0.10	0.17	0.11
ω_d (Hz)	62.83	36.96	57.12
δ	0.430	0.723	0.300
ζ	0.068	0.114	0.048
ω_n (Hz)	62.98	37.06	57.19

**Figure 4.4** Decay of the impulse given to the system

4.3 Self-Induced Pitching Oscillations

4.3.1 Parameters of the study

The self-induced oscillations of a NACA 0012 airfoil have been investigated under a set of parameters which are summarized as follows:

- *Stiffness of the system*: three different springs have been used. The stiffness values are reported in § 4.2 in terms of the natural frequency of the system as $\omega_n \cong 37$ Hz, 57 Hz and 63 Hz.
- *Freestream velocity*: the flow speed has been adjusted to an approximately common minimum, maximum and an intermediate value to observe oscillations

when the other parameters are fixed. The actual lower and upper limits for freestream velocities to observe oscillations have also been determined and can be deduced from Figure 4.5. As the freestream velocity is determined precisely during each experiment, it may vary up to 10% in a category. Although there exists some discrepancy, the minimum freestream velocity corresponds to a Reynolds number around $Re = 7.5 \times 10^4$, the intermediate is around $Re = 11 \times 10^4$ and the maximum around $Re = 14.5 \times 10^4$. The change in the freestream combined with the resulting oscillation frequency affects the reduced frequency of the case ranging from $\omega_r = 0.26$ to 0.49 . According to the review of McCroskey [1], all the cases investigated are in deep stall region and beyond.

- *Initial angle of attack*: the airfoil is positioned to a set of angles of attack, i.e., $\alpha = 0^\circ, 10^\circ, 20^\circ$ and 25° , before the wind tunnel is operated. Depending on the freestream velocity and the stiffness of the system, this initial value changes a little bit and tends to be around $0^\circ, 7^\circ, 9^\circ$ and 11° , which will be named thereafter in this study as Angle-0, Angle-1, Angle-2 and Angle-3. Then the airfoil is let to oscillate and it undergoes nearly sinusoidal oscillations which can be represented simply by $\alpha(t) = \alpha_0 + \alpha_{ampl} \cos \omega t$. The results indicate that α_0 is not necessarily equal to the initial angle of attack. The experiments performed with an initial zero angle of attack do not yield visible or detectable oscillations and therefore corresponding results are not included in this thesis.

4.3.2 Acceleration measurements

The summary of the results is given in Table 4.6 and is plotted in Figure 4.5. The frequency of oscillations increases as the Reynolds number increases at each natural frequency of the system.

Time traces of acceleration have been given in Appendix B1, for a period of 5 seconds in Figures B1.2 to B1.4 and for a period of 1 second in Figures B1.5 to B1.7, corresponding to approximately 8 to 15 and 40 to 75 cycles of oscillation respectively depending on the resulting frequency of oscillations. Both sets of figures indicate locked-in oscillations for angles of attack larger than 7° . On the other hand, the oscillations cease for the lowest Reynolds number when the initial angle of attack

Table 4.6 Cases of the study and corresponding values of the parameters

	Case Code	Freestream Velocity		Re	f osc. Hz	ω_r
		Mean m/s	St. Dev.			
Spring 1 ($\omega_n=62.98$ Hz)	s1a0t1	8.85	0.191	76335	X	X
	s1a1t1	9.00	0.209	77629	X	X
	s1a2t1	8.72	0.121	75189	10.82	0.4679
	s1a3t1	8.30	0.430	71570	X	X
	s1a0t2	13.01	0.167	112187	X	X
	s1a1t2	12.81	0.114	110487	X	X
	s1a2t2	12.77	0.134	110149	12.67	0.3740
	s1a3t2	12.64	0.190	109028	13.00	0.3877
	s1a0t3	17.04	0.093	147009	X	X
	s1a1t3	17.08	0.160	147291	X	X
	s1a2t3	17.13	0.155	147725	14.11	0.3106
	s1a3t3	16.92	0.132	145976	14.76	0.3288
	s1a3tx2_6	10.76	0.240	92812	12.08	0.4232
	s1a2tx1_75	8.49	0.245	73223	10.58	0.4698
	Case Code	Freestream Velocity		Re	f osc. Hz	ω_r
		Mean m/s	St. Dev.			
Spring 2 ($\omega_n=37.06$ Hz)	s2a0t1	8.86	0.230	76382	X	X
	s2a1t1	8.45	0.114	72820	8.16	0.3640
	s2a2t1	8.15	0.205	70218	8.73	0.4039
	s2a3t1	8.14	0.303	70168	X	X
	s2a0t2	12.76	0.097	109997	X	X
	s2a1t2	12.70	0.082	109421	9.82	0.2915
	s2a2t2	13.01	0.123	112094	10.27	0.2976
	s2a3t2	12.51	0.150	107768	10.89	0.3283
	s2a0t3	16.83	0.092	145053	X	X
	s2a1t3	16.79	0.084	144646	11.67	0.2621
	s2a2t3	17.16	0.106	147869	12.07	0.2652
	s2a3t3	16.48	0.123	141981	12.96	0.2965
	s2a3tx2_4	9.83	0.178	84714	9.96	0.3819
	s2a2tx1_6	7.00	0.114	60356	8.31	0.4473
	s2a1tx1_6	6.87	0.178	59175	7.8	0.4282
	Case Code	Freestream Velocity		Re	f osc. Hz	ω_r
		Mean m/s	St. Dev.			
Spring 3 ($\omega_n=57.19$ Hz)	s3a0t1	9.05	0.274	78111	X	X
	s3a1t1	8.81	0.165	76063	10.08	0.4312
	s3a2t1	8.63	0.101	74512	10.96	0.4786
	s3a3t1	8.70	0.130	75066	X	X
	s3a0t2	12.96	0.098	111872	X	X
	s3a1t2	12.75	0.089	110072	11.24	0.3322
	s3a2t2	12.83	0.164	110762	12.51	0.3675
	s3a3t2	12.67	0.145	109363	12.64	0.3760
	s3a0t3	16.90	0.117	145834	X	X
	s3a1t3	16.95	0.154	146297	12.6	0.2802
	s3a2t3	16.98	0.095	146566	13.73	0.3048
	s3a3t3	16.76	0.116	144650	14.51	0.3264
	s3a3tx2_7	11.10	0.136	95833	11.82	0.4013
	s3a2tx1_9	7.96	0.158	68696	10.42	0.4935
	s3a1tx1_9	8.21	0.294	70859	9.78	0.4491

Case Codes;

s: spring; 1 $\rightarrow \omega_n=62.98$ Hz, 2 $\rightarrow \omega_n=37.06$ Hz, 3 $\rightarrow \omega_n=57.19$ Hz

a: initial angle of attack; 0 $\rightarrow \alpha=0^\circ$, 1 $\rightarrow \alpha=7^\circ$, 2 $\rightarrow \alpha=9^\circ$, 3 $\rightarrow \alpha=11^\circ$

t: freestream velocity; 1(knob position:2) $\rightarrow Re \approx 7.5 \times 10^4$,

2(knob position:3) $\rightarrow Re \approx 11 \times 10^4$, 3(knob position:4) $\rightarrow Re \approx 14.5 \times 10^4$

tx: knob position to adjust the freestream velocity.

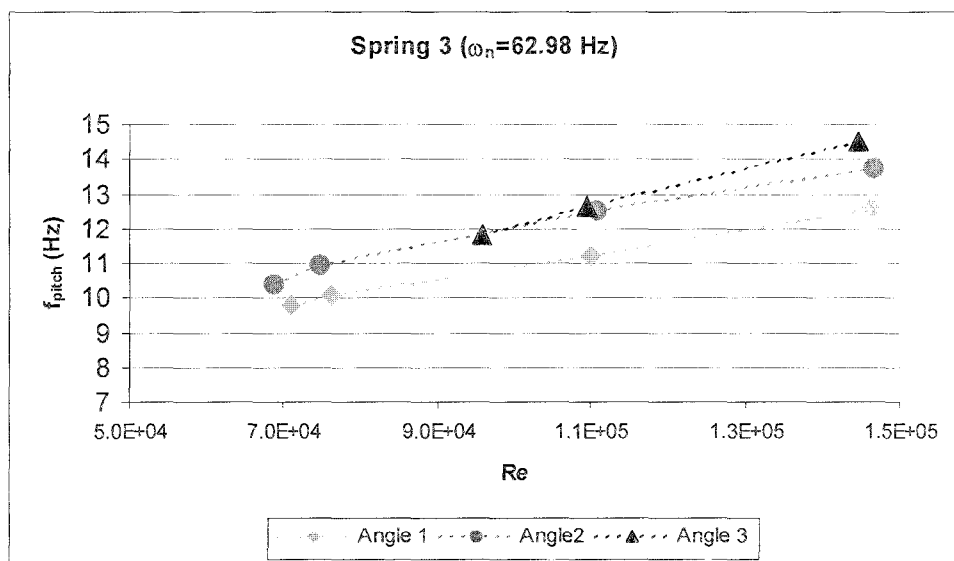
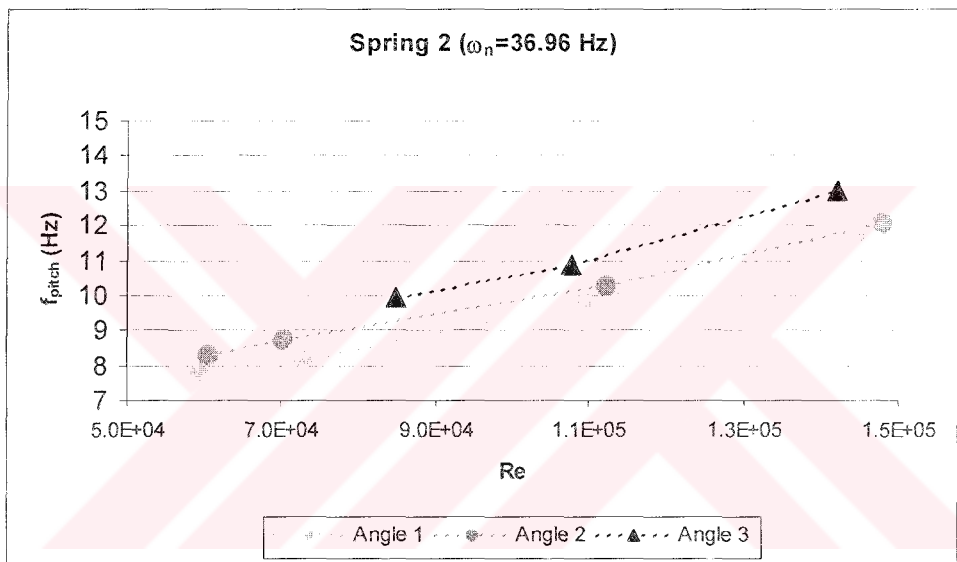
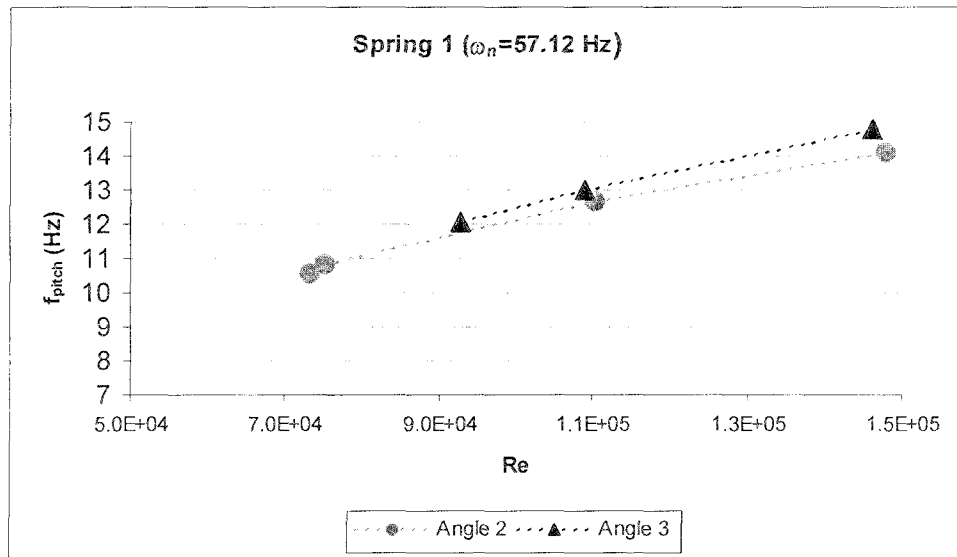


Figure 4.5 Pitching frequencies with respect to Reynolds number

is larger than 10° . Except for the lowest Reynolds number case when the airfoil is at an angle of attack around 9° , the acceleration signals are highly modulated.

The spectra of acceleration have been obtained for all cases and are given in Figure B1.8. The frequency axis have also been normalized with corresponding reduced frequencies to determine any relation for the harmonics of the acceleration signal. Although Figure B1.9 indicates no relation in between, it is evident that most of the cases exhibit at least three harmonics and the first occurs around 40 times the reduced frequency. The first and the following peaks increase in frequency with increasing Reynolds number. Combined observation of the spectra and time histories reveals that for an initial angle of attack around 9° , the acceleration signal of the lowest Reynolds number cases exhibits a much more sinusoidal like behavior with less pronounced modulations. An integration procedure has been successfully applied to one of them to yield the angular velocity and angular motion of the airfoil.

4.3.3 PIV measurements and vortex formation around the airfoil

Vorticity distributions corresponding to local or absolute maximum and minimum peaks for different modulated acceleration signals have been presented in Figures B2.1 to B2.8. Three images of vortex formation for each selected peak have been obtained to show the repeatability of the data and periodicity of the flow. Figure B2.1 presents the case where there is a light modulation of the acceleration signal around its minimum value. A stall vortex is in evolution when the acceleration signal travels from its minimum to its maximum and is shed when it reaches its maximum. A negative counter rotating trailing edge vortex (TEV) is evident when the stall vortex covers approximately half of the chord length.

The modulation of the acceleration signal around its minimum is more pronounced in Figure B2.2. In this case, the correlation yields a similar scenario, the stall vortex starts to form, covers more than half of the chord length when the acceleration reaches a local maximum and is shed when the acceleration is at its maximum. The negative trailing edge vortex is more pronounced compared to the previous case when the acceleration is at its minimum.

Figures B2.1 and B2.2 are selected from the cases obtained with the first spring with $\omega_n \cong 63$ Hz. When the natural frequency of the system is much lower, i.e. $\omega_n \cong 37$ Hz, a similar correlation can be made. Figure B2.3 can be compared with Figure B2.1; except for the natural frequency of the system, the other parameters are the same. Although the acceleration signal is slightly different, the occurrence of the stall vortex formation and shedding corresponds to the same acceleration trend. Perhaps the only difference is that the stall vortex does not start to form when the acceleration reaches its first local minimum after its maximum. However, the minimum value of acceleration does not happen just after the maximum, instead it is followed by the maximum.

Similarly Figure B2.4 can be compared with Figure B2.2. The difference in the acceleration modulation is greater, the decrease in the natural frequency of the system causes additional local peaks to form. The stall vortex starts to form on the first local minimum of the acceleration and continues to grow until the minimum is reached. The signs of shedding are evident before the minimum of the acceleration signal. A major difference is that the maximum angle of attack is slightly lower, the stall vortex does not cover more than 2/3 of the suction side and the counter rotating trailing edge vortex can not be captured on the airfoil, it is detectable in the wake of the airfoil.

When the system's natural frequency is slightly higher than the first case in consideration, i.e., the case presented in Figure B2.1, the results in Figure B2.5 show that neither the acceleration nor the vortex formation patterns are affected. This observation is made for the lowest Reynolds number. However, the acceleration modulations become accentuated when the natural frequency of the system is increased from $\omega_n \cong 57$ Hz to $\omega_n \cong 63$ Hz for the intermediate Reynolds number cases. An example is given in Figure B2.6 where the acceleration signal exhibits additional local peaks. There are two local maximums and minimums; however the signal is different than what is observed in Figure B2.4, local peaks do not have approximately the same values, following the maximum, local maximums are gradually decreasing or local minimums are gradually increasing until the minimum. Correlation of vortex formation patterns yields that the stall vortex grows starting from the first local minimum until the absolute one is reached. Its form is slender

than what we observed in Figure B2.2 and its length surpasses almost the trailing edge before it is shed.

The same cases, presented in Figure B2.5 and B2.6, are investigated with a difference in the initial angle of attack and, representative images along with the acceleration signals and corresponding spectra are given in Figure B2.7 and B2.8. Although the cases are not as much locked-on as the previous ones, the occurrence of the local peaks are different, they follow the minimum instead of the maximum. In general the vortex formation patterns are also different than the previous cases. Actually the formation of the stall vortex starts similarly at the first minimum after the maximum and it is shed before the maximum is reached. However, the formation of a negative vortex on pressure side is evident especially in Figure B2.8, the shed vortices and separating shear layers are clearly detectable in the near wake.

Figure B3.1 to B3.3 visualize a period of oscillation in detail in terms of vorticity patterns. Figure B3.1 reveals clearly that the stall vortex is shed when the acceleration is increasing from its minimum value to its maximum and when it is about zero. The start of its formation is detected when the acceleration decreases from its maximum and is around zero. Although the scenario is the same in general for the cases presented in Figure B3.2 and B3.3, local peaks announce a kind of intermediate shedding. The last positive peak before the minimum in Figure B3.2 or in Figure B3.3 corresponds to an intermediate shedding before the major one occurs just before the maximum acceleration is obtained. The acceleration will be zero when the velocity is either maximum or minimum; therefore it is possible to conclude that both the formation start and the shedding of the stall vortex occur when the airfoil velocity is maximum or minimum. Two integration methods have been used to obtain the position of the airfoil from the acceleration data. First one is a numerical integration based on the trapezoidal rule. The second is based on the reproduction of the acceleration signal with the major frequency peaks determined from its spectrum. The second integration method needs an initial condition for velocity and position. To exclude any none harmonic terms in the equation representing the position, the initial velocity is determined as zero. On the other hand one of the PIV images has been used to set the initial condition for the position. The other images confirm the angular position obtained by the integration. Figure B3.4 represents the results of the integration for the selected case. As can be seen on the graph, the angular position of

the airfoil changes between approximately $+27^\circ$ and -4° , the mean value is 10.5° . Although the case is titled as an Angle-2 case, the pictures taken before the airfoil is let to undergo oscillations indicate that the initial angle of attack is 11.2° . The case is actually discussed first regarding the vortex formation in correlation with the acceleration data with Figure B2.1. It is now possible to conclude that the formation of the stall vortex starts just after the mean value on the increasing angle of attack direction and the stall vortex is shed just after the mean value on the opposite direction.



5 CONCLUDING REMARKS

Self-induced pitching oscillations of a NACA 0012 airfoil are investigated using digital particle image velocimetry in conjunction with instantaneous acceleration measurements. The vortex formation patterns are obtained for different natural frequencies of the system, at different Reynolds numbers and with different initial angle of attack of the airfoil. The major remarks are as follows:

- Both the suction and pressure side of the airfoil have been visualized
- Self-induced oscillations are obtained for almost all the cases investigated. However, high frequency of oscillations did not allow capturing in detail a cycle of oscillation with the current camera speed.
- The terms in the equation of motion have been obtained through analytical integration of the acceleration data. However, some conditioners have the capability to perform such integration during the acquisition, which will solve the problem of determining the initial conditions. Determination of velocity and displacement via integration of the acceleration data requires at least one PIV image to evaluate an initial condition.
- The vortex formation patterns are correlated with the acceleration signal. It has been observed that the small modulations correspond to some intermediate shedding. Especially the shedding of the stall vortex is correlated with the local or absolute minimum before the absolute maximum on the acceleration signal. As the angular position of the airfoil could be determined via integration of acceleration, it is possible to state that the formation of the stall vortex starts just after the mean value when the angle of attack is increasing and the stall vortex is shed just after the mean value is attained when the angle of attack is decreasing.

The study showed that the equation of motion can be set and compared with any moment prediction via PIV. On the other hand, since it is crucial to obtain $C_m - \alpha$ curves to determine the direction of the energy transfer for oscillating airfoils, further study will include the analysis of the moments and their correlation with vortex formations. For future work, in order to increase the scope of the investigation, reducing the frequency of self-induced oscillations and integration of the acceleration during its acquisition should be the first goals of the experiments.



REFERENCES

- [1] **McCroskey, W. J.**, 1982. Unsteady Airfoils, *Annual Review of Fluid Mechanics*, **14**, 285-311.
- [2] **Panda, J. and Zaman, K. B. M. Q.**, 1994. Experimental Investigation of the Flow Field of an Oscillating Airfoil and Estimation of Lift From Wake Surveys, *Journal of Fluid Mechanics*, **265**, 65-95.
- [3] **Lighthill, J.**, 1986. Fundamentals Concerning Wave Loading on Offshore Structures, *Journal of Fluid Mechanics*, **173**, 667-681.
- [4] **Sarpkaya, T.**, 1975. An Inviscid Model of Two-Dimensional Vortex Shedding for Transient and Asymptotically Steady Separated Flow Over an Inclined Plate, *Journal of Fluid Mechanics*, **68**, 109-128.
- [5] **Noca, F.**, 1997. On the Evaluation of Time-Dependent Fluid-Dynamic Forces on Bluff Bodies, *PhD Thesis*, California Institute of Technology.
- [6] **Noca, F., Shiels, D. and Jeon, D.**, 1997. Measuring Instantaneous Fluid Dynamic Forces on Bodies, Using Only Velocity Fields and Their Derivatives, *Journal of Fluids and Structures*, **11**, 345-350.
- [7] **Lin, J. C. and Rockwell, D.**, 1996. Force Identification by Vorticity Fields: Techniques Based on Flow Imaging, *Journal of Fluids and Structures*, **10**, 663-668.
- [8] **Lin, J. C. and Rockwell, D.**, 1999. Horizontal Oscillations of a Cylinder Beneath a Free Surface: Vortex Formation and Loading, *Journal of Fluid Mechanics*, **389**, 1-26.
- [9] **Zhu, Q., Lin, J. C., Unal, M. F. and Rockwell, D.**, 2000. Motion of a Cylinder Adjacent to a Free-Surface: Flow Patterns and Loading, *Experiments in Fluids*, **28(6)**, 559-575.
- [10] **Yuan, J.**, 2002. Circulation Methods in Unsteady and Three-Dimensional Flows, *PhD Thesis*, Faculty of the Worcester Polytechnic Institute.
- [11] **Kramer, M.**, 1932. Increase in the Maximum Lift of an Airfoil due to a Sudden Increase in its Effective Angle of Attack Resulting from a Gust, *NASA Tech. Memorandum*, **678**.

- [12] **McCroskey, W. J.**, 1972. Detailed Aerodynamic Measurements on a Model Rotor in the Blade Stall Regime, *Journal of the American Helicopter Society*, **17**, 20-30.
- [13] **Carr, L. W., McAlister, K. W. and McCroskey, W. J.**, 1977. Analysis of Dynamic Stall Based on Oscillating Airfoils Experiments, *NASA TN*, **D-8382**.
- [14] **Ruyck, J. De and Hirsch, C.**, 1983. Instantaneous Turbulence Profiles in the Wake of an Oscillating Airfoil, *AIAA Journal*, **21(5)**, 641-642.
- [15] **Kim, J. S. and Park, S. O.**, 1988. Smoke Wire Visualization of Unsteady Separation Over an Oscillating Airfoil, *AIAA Journal*, **26(11)**, 1408-1410.
- [16] **Park, S. O., Kim, J. S. and Lee, B. I.**, 1990. Hot-Wire Measurements of Near Wakes Behind an Oscillating Airfoil, *AIAA Journal*, **28(1)**, 22-28.
- [17] **Leishman, J. G.**, 1990. Dynamic Stall Experiments on the NACA 23012 Aerofoil, *Experiments in Fluids*, **9**, 49-58.
- [18] **Lee, T., Petrakis, G., Mokhtarian, F. and Kafyeke, F.**, 1999. Boundary-Layer Transition, Separation and Reattachment on an Oscillating Airfoil, *Journal of Aircraft*, **37(2)**, 356-360.
- [19] **Shih, C. and Ho, C. M.**, 1994. Vorticity Balance and Time Scales of a Two-Dimensional Airfoil in an Unsteady Free Stream, *Physics of Fluids*, **6(2)**, 710-723.
- [20] **Shih, C., Lourenco, L., Dommelen, L. V. and Krothapalli, A.**, 1992. Unsteady Flow Past an Airfoil Pitching at a Constant Rate, *AIAA Journal*, **30(5)**, 1153-1161.
- [21] **Raffel, M., Kompenhans, J. and Wernert, P.**, 1995. Investigation of the Unsteady Flow Velocity Field Above an Airfoil Pitching Under Deep Dynamic Stall Conditions, *Experiments in Fluids*, **19**, 103-111.
- [22] **Wernert, P., Geissler, W., Raffel, M. and Kompenhans, J.**, 1996. Experimental and Numerical Investigations of Dynamic Stall on a Pitching Airfoil, *AIAA Journal*, **34(5)**, 982-989.
- [23] **Wernert, P., Koerber, G., Wietrich, F., Raffel, M. and Kompenhans, J.**, 1997. Demonstration by PIV of the Non-Reproducibility of the Flow Field Around an Airfoil Pitching Under Deep Dynamic Stall Conditions and Consequences Thereof, *Aerospace Science and Technology*, **2**, 125-135.
- [24] **Oshima, H. and Ramaprian, B. R.**, 1997. Velocity Measurements over a Pitching Airfoil, *AIAA Journal*, **35(1)**, 119-126.
- [25] **Acar, H.**, 1991. Akım Ayrılması, *Yüksek Lisans Tezi*, İ.T.Ü. Fen Bilimleri Enstitüsü, İstanbul.

- [26] **Chyu, C. K.**, 1995. A Study of the Near-Wake Structure From a Circular Cylinder, *PhD Thesis*, Lehigh University, Bethlehem.
- [27] **Landreth, C. C. and Adrian, R. J.**, 1989. Measurement and Refinement of Velocity Data Using High Image Density Analysis in Particle Image Velocimetry, *Applications of Laser Anemometry: Proceedings of the 4th International Symposium*, Eds. R. J. Adrian, T. Asunuma, D. Durao, F. Durst and J. Whitlaw, Springer Verlag, Berlin, 484-497.
- [28] **Hodges, D. H. and Pierce, G. A.**, 2002. Introduction to Structural Dynamics and Aeroelasticity, Cambridge University Press, Cambridge.



APPENDIX A

DETERMINATION OF NATURAL FREQUENCY

Natural frequency of a system can be obtained by the damping test. Necessary parameters for the calculations are found from the decay of the impulse given to the system. T_d ; period of free underdamped vibrations is the amount of time that the system takes to execute each cycle. Then the damped natural frequency, ω_d , is given by;

$$\omega_d = \frac{2\pi}{T_d} \quad (\text{A1.1})$$

Logarithmic decrement, δ , is the natural logarithm of the ratio of the amplitudes of vibration on successive cycles and can be written as;

$$\delta = \ln\left(\frac{\ddot{x}(t)}{\ddot{x}(t+T_d)}\right) \quad (\text{A1.2})$$

Then the damping ratio, ζ , can be expressed as;

$$\zeta = \frac{\delta}{\sqrt{4\pi^2 + \delta^2}} \quad (\text{A1.3})$$

Finally, the natural frequency is determined by;

$$\omega_d = \omega_n \sqrt{1 - \zeta^2} \quad (\text{A1.4})$$

APPENDIX B1

TIME HISTORIES AND SPECTRA OF ACCELERATION SIGNALS



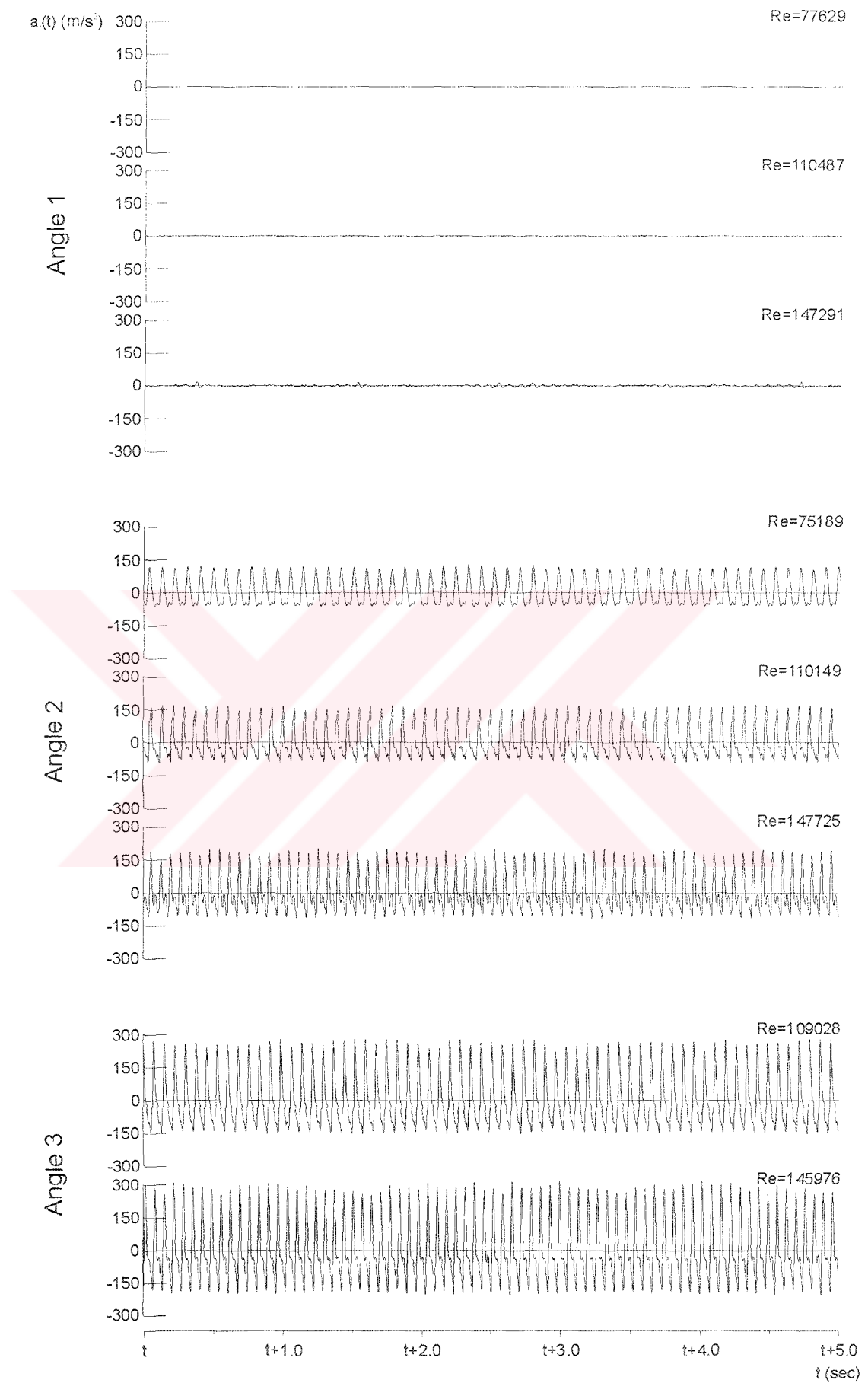


Figure B1.1 Time traces of acceleration for a period of 5 seconds. (Spring 1)

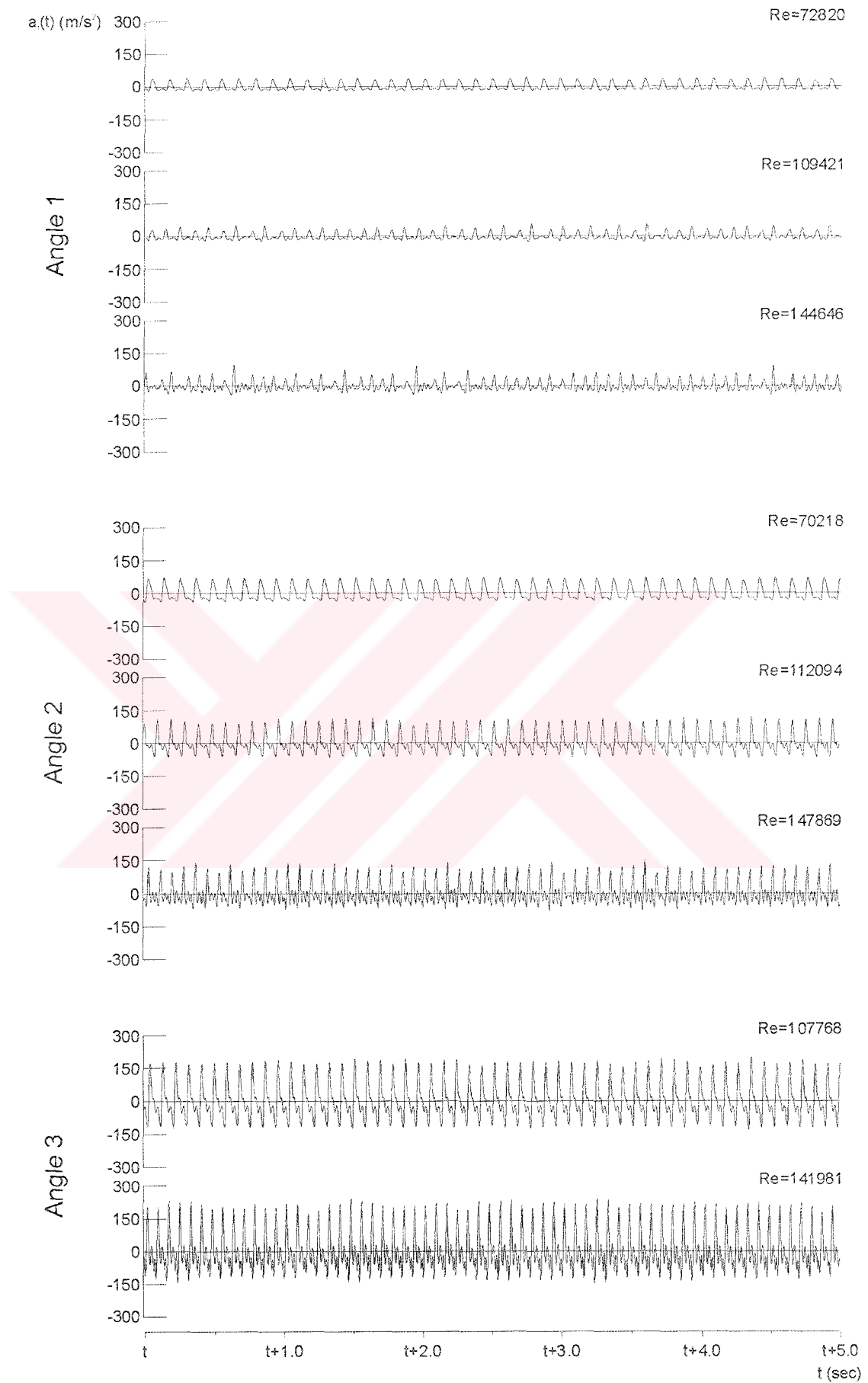


Figure B1.2 Time traces of acceleration for a period of 5 seconds. (Spring 2)



Figure B1.3 Time traces of acceleration for a period of 5 seconds. (Spring 3)

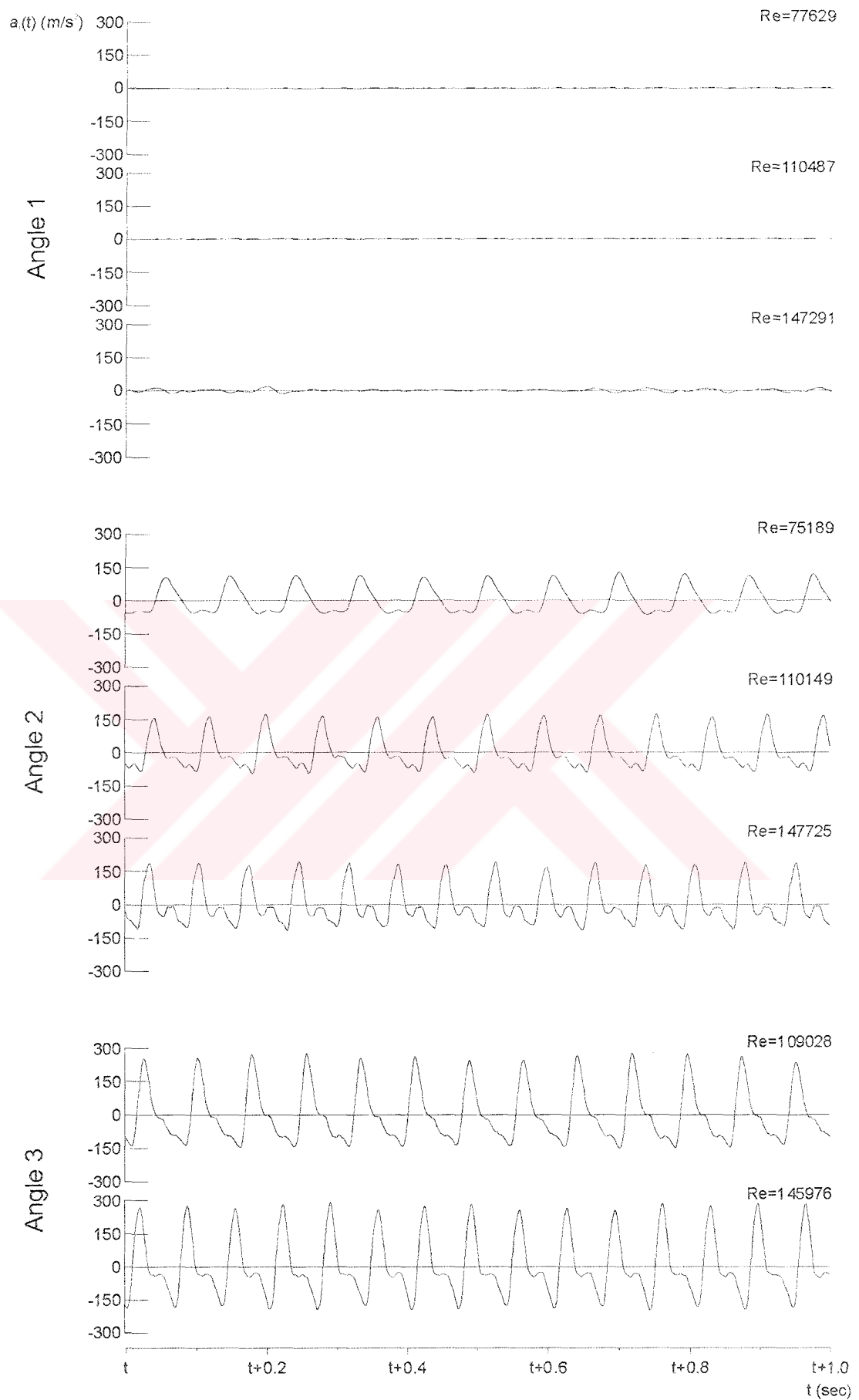


Figure B1.4 Time traces of acceleration for a period of 1 second. (Spring 1)

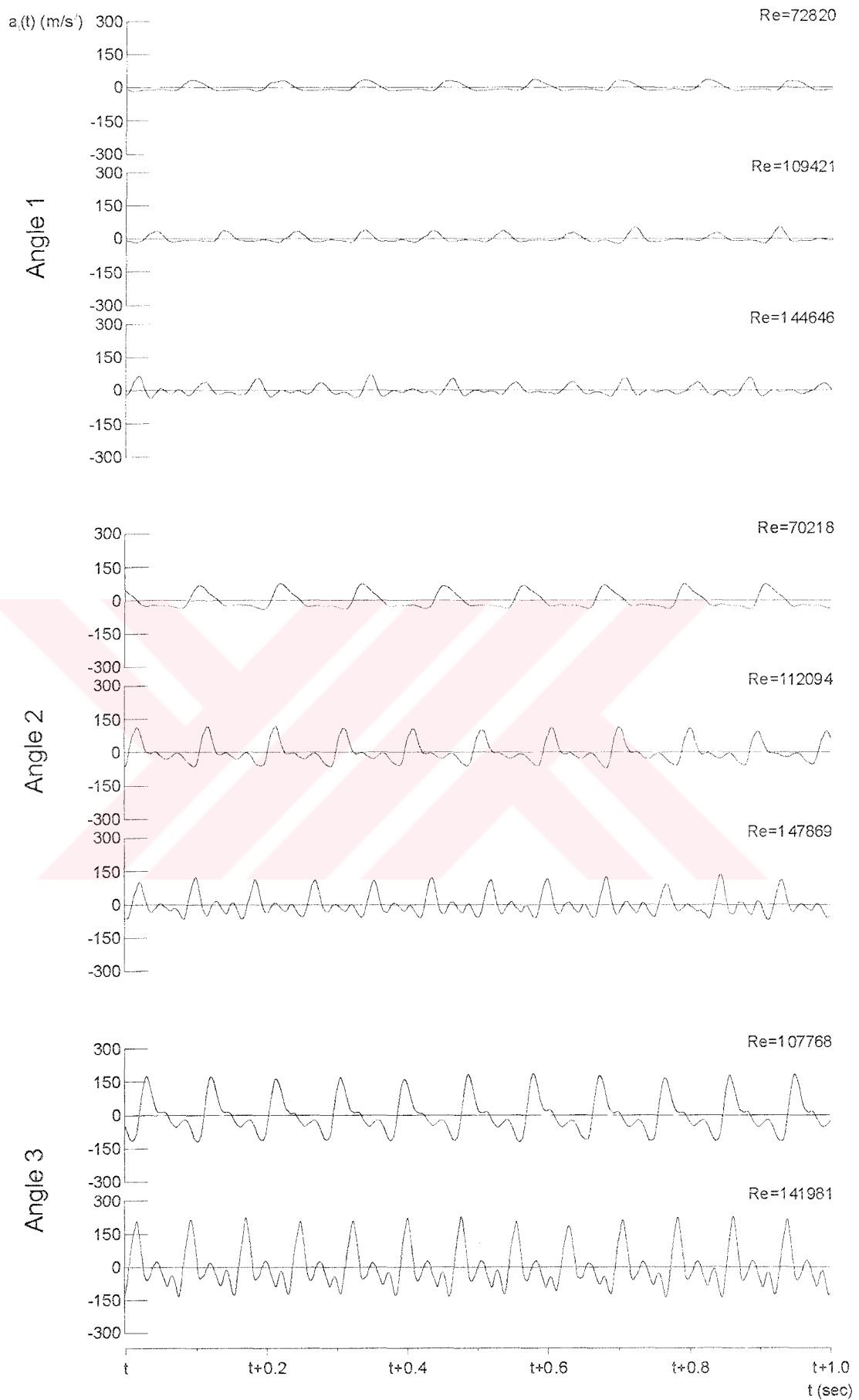


Figure B1.5 Time traces of acceleration for a period of 1 second. (Spring 2)



Figure B1.6 Time traces of acceleration for a period of 1 second. (Spring 3)

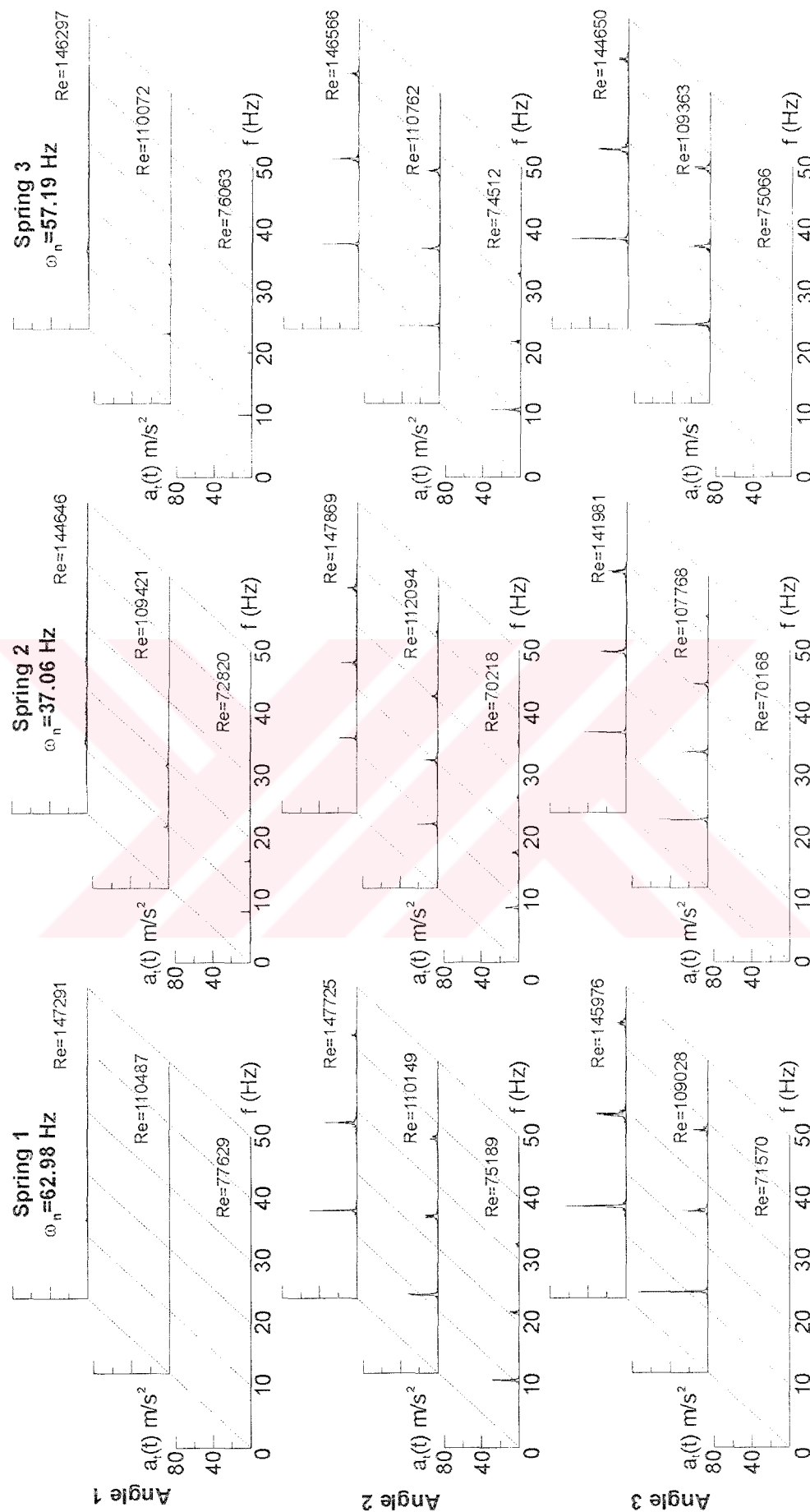


Figure B1.7 Spectra of acceleration.

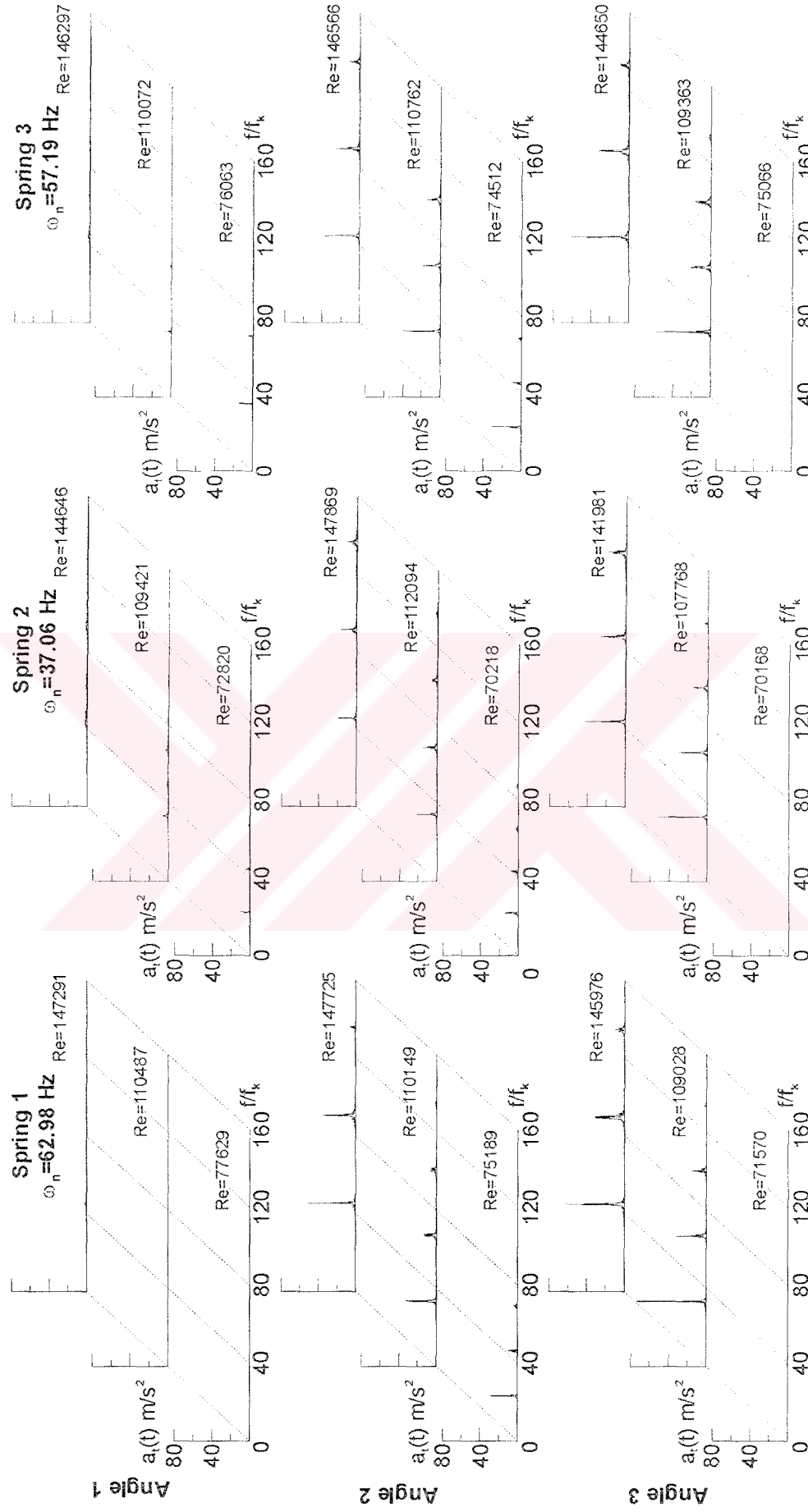


Figure B1.8 Spectra of acceleration. (Frequency axis is non-dimensionalized with corresponding reduced frequencies)

APPENDIX B2

VORTICITY FORMATION AROUND THE AIRFOILS AND CORRESPONDING INSTANTANEOUS ACCELERATION OF THE AIRFOILS



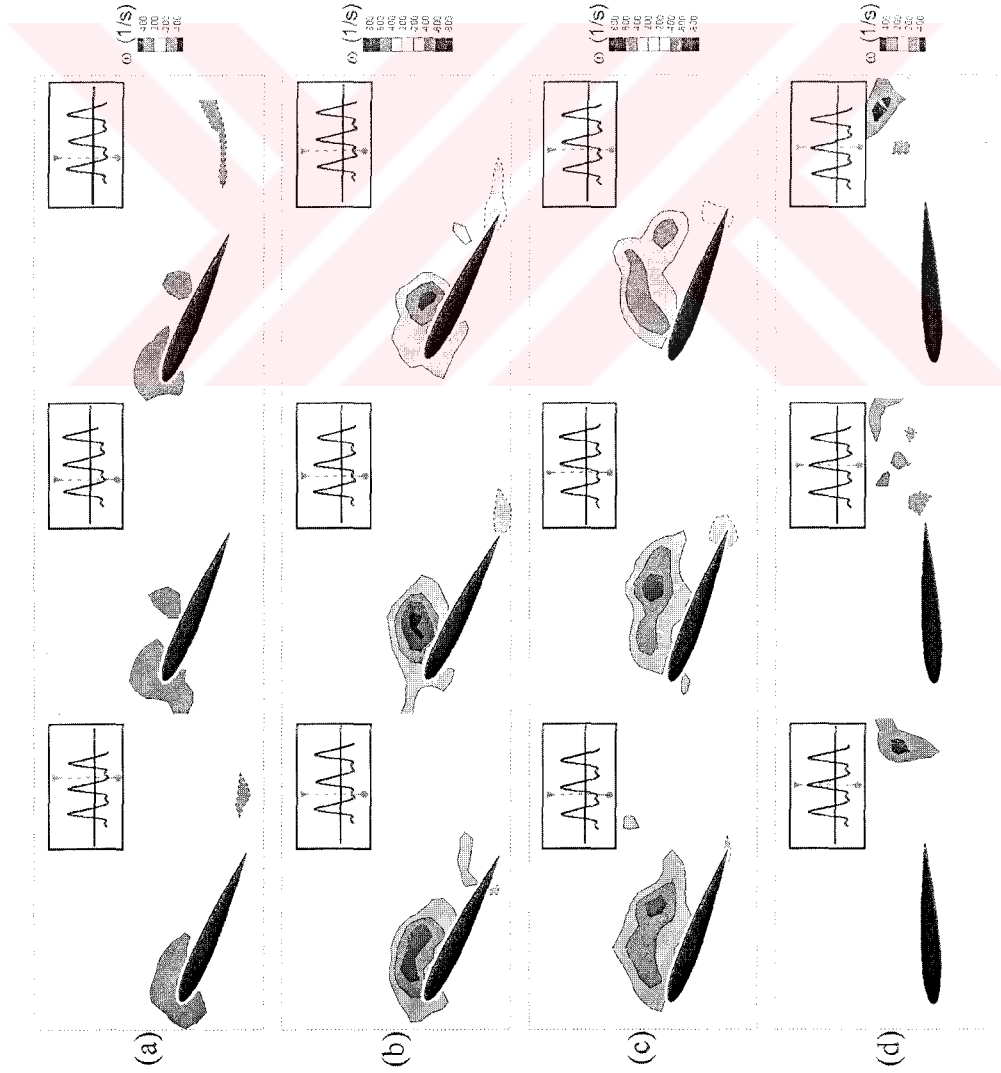
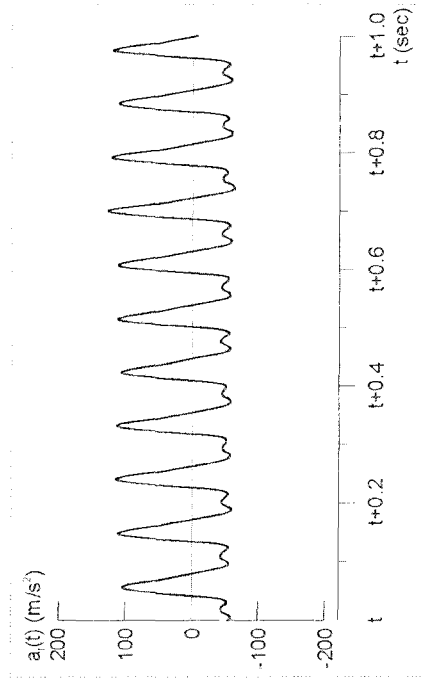
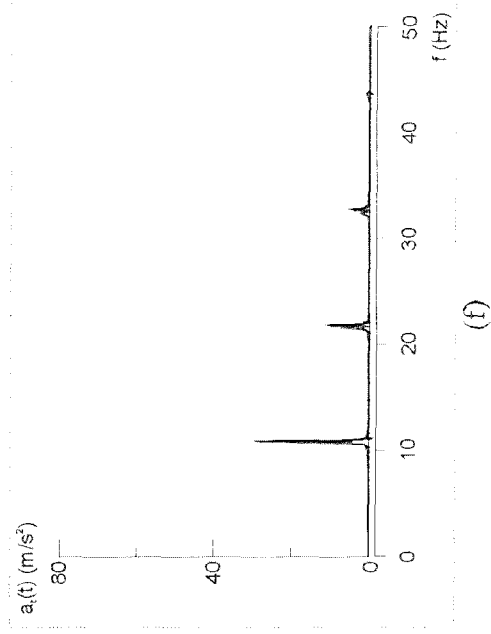


Figure B2.1 Selected 3 images of vorticity patterns for oscillations at $Re = 75,189$ with Spring 1 ($\alpha_{int} = \text{Angle } 2$)

a) $\alpha_{inst} = 24^\circ$ b) $\alpha_{inst} = 27^\circ$ c) $\alpha_{inst} = 20^\circ$ d) $\alpha_{inst} = -3^\circ$
and corresponding acceleration - time trace (e) and acceleration spectra (f) graphs.



(e)



(f)

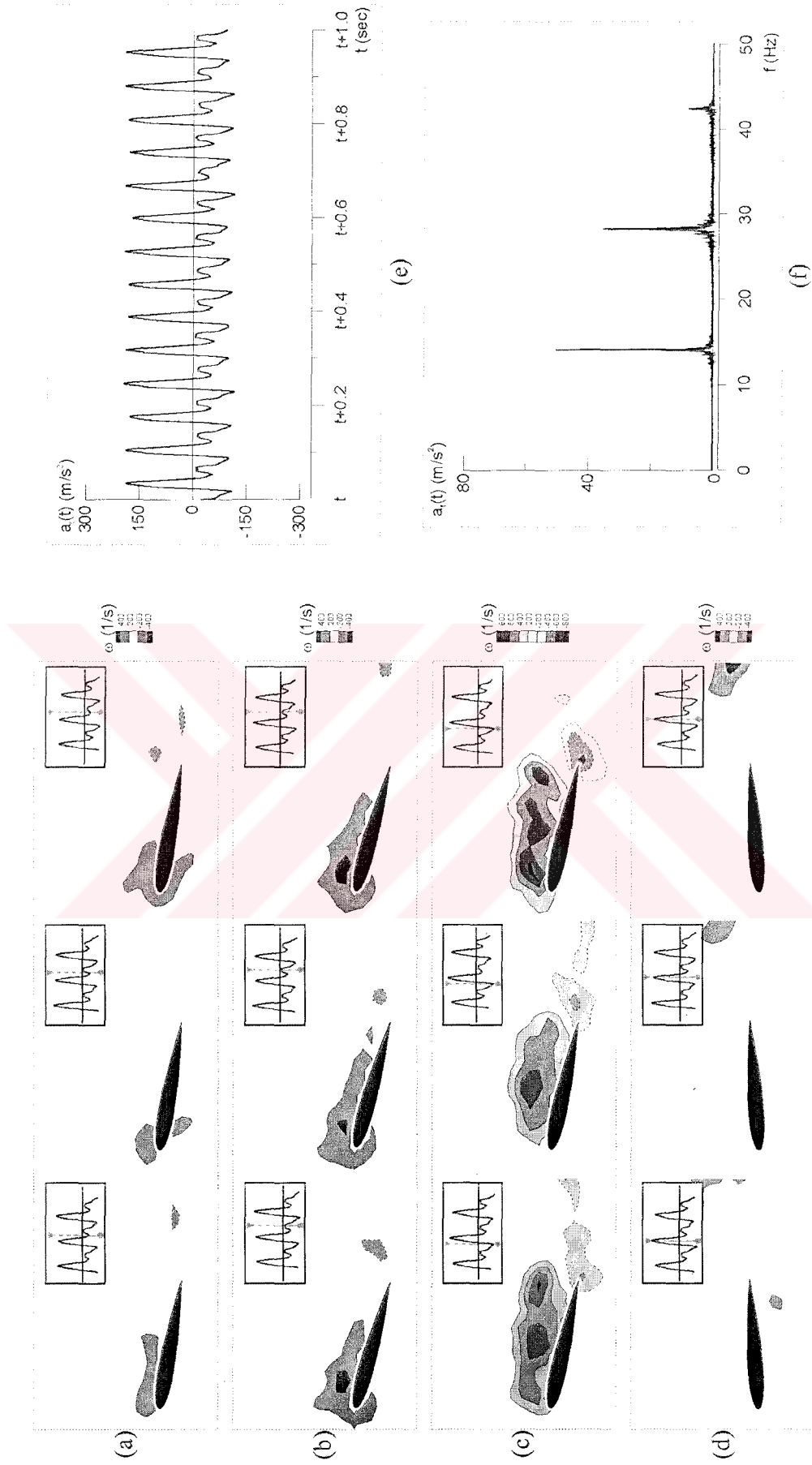


Figure B2.2 Selected 3 images of vorticity patterns for oscillations at $Re = 147,725$ with Spring 1 ($\alpha_{inst} = \text{Angle } 2$)

a) $\alpha_{inst} = 10^\circ$ b) $\alpha_{inst} = 16^\circ$ c) $\alpha_{inst} = 12^\circ$ d) $\alpha_{inst} = -4^\circ$
and corresponding acceleration - time trace (e) and acceleration spectra (f) graphs.

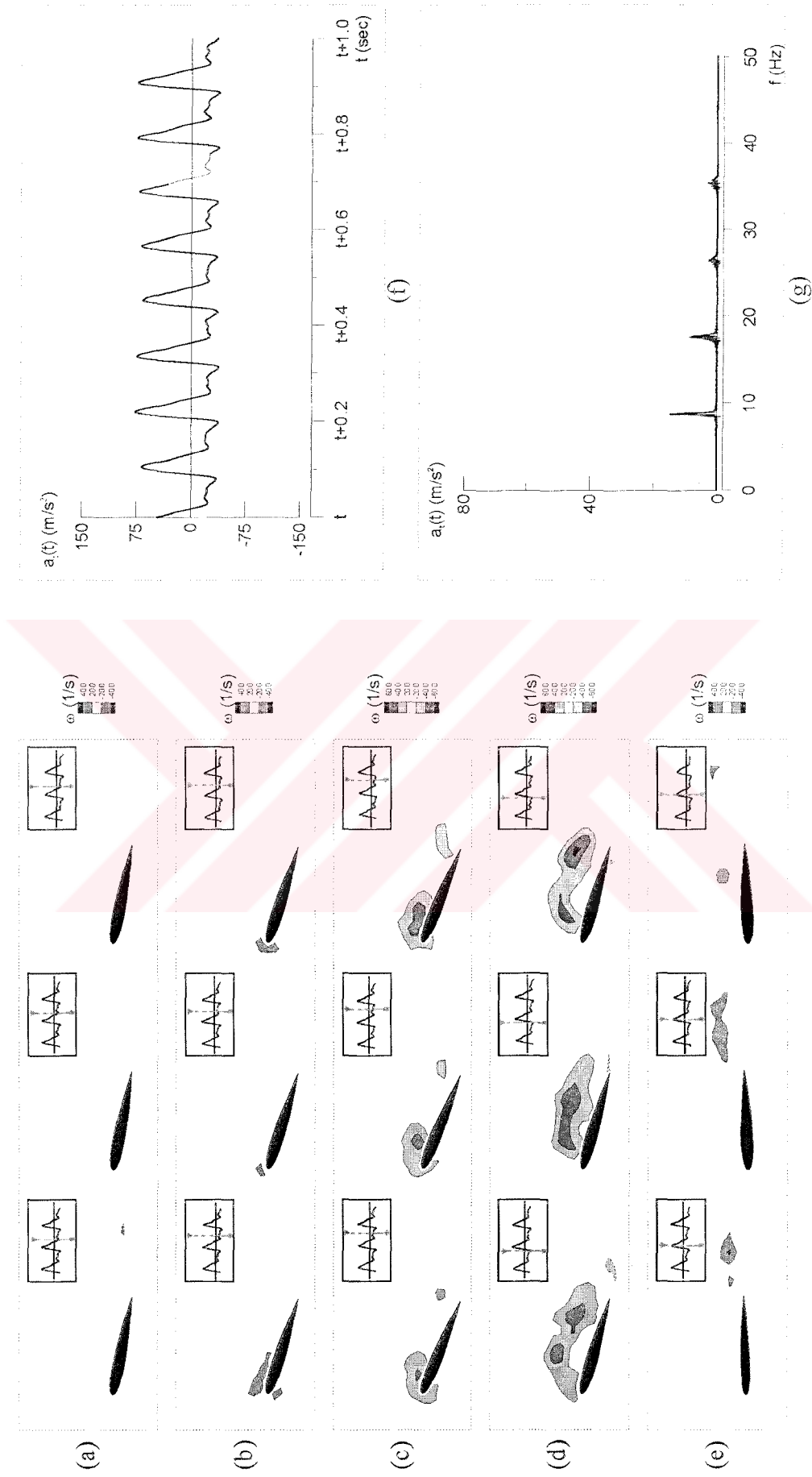


Figure B2.3 Selected 3 images of vorticity patterns for oscillations at $Re = 70,218$ with Spring 2 ($\alpha_{init} = \text{Angle } 2$)

a) $\alpha_{inst} = 11^\circ$ b) $\alpha_{inst} = 18^\circ$ c) $\alpha_{inst} = 22^\circ$ d) $\alpha_{inst} = 16^\circ$ e) $\alpha_{inst} = -2^\circ$

and corresponding acceleration - time trace (f) and acceleration spectra (g) graphs.

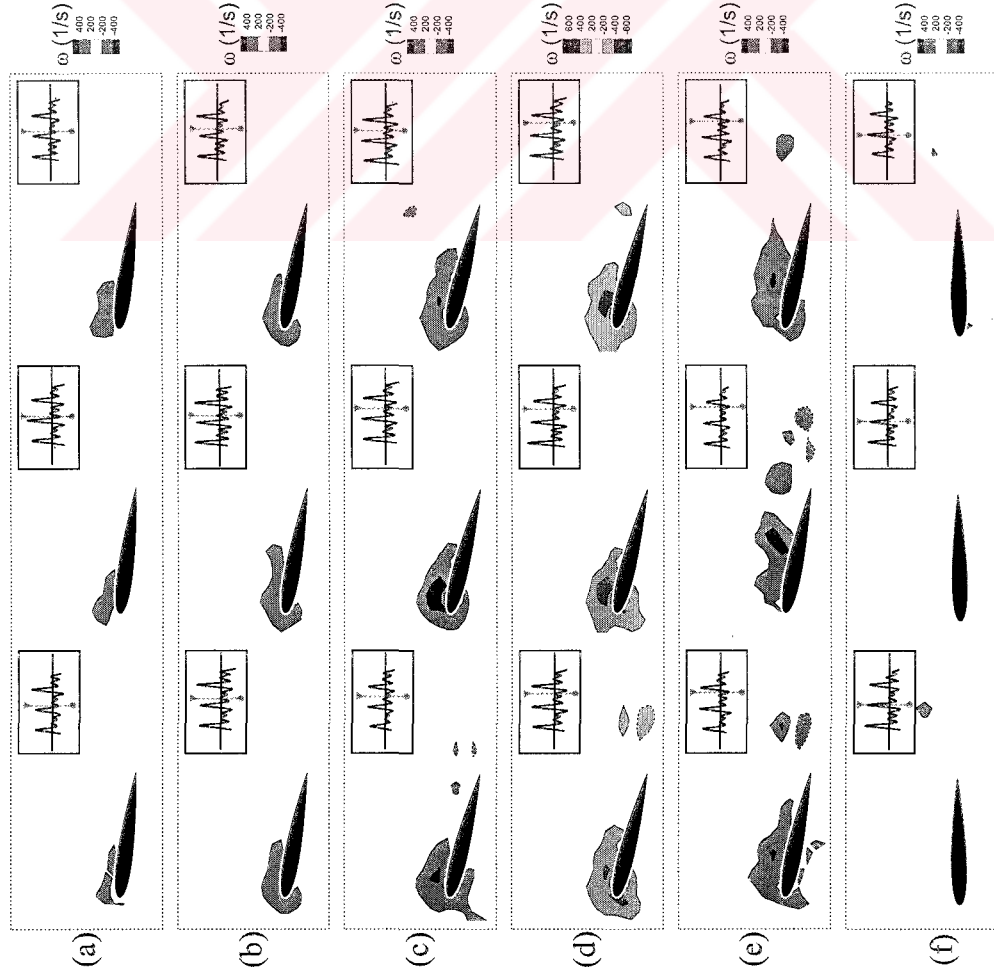
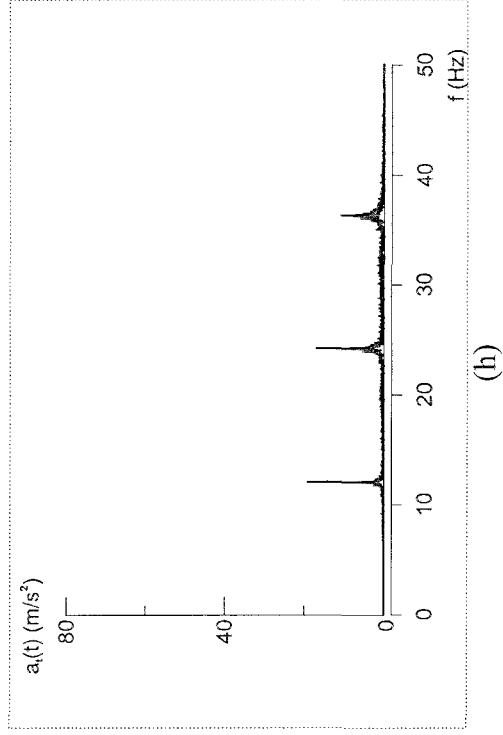
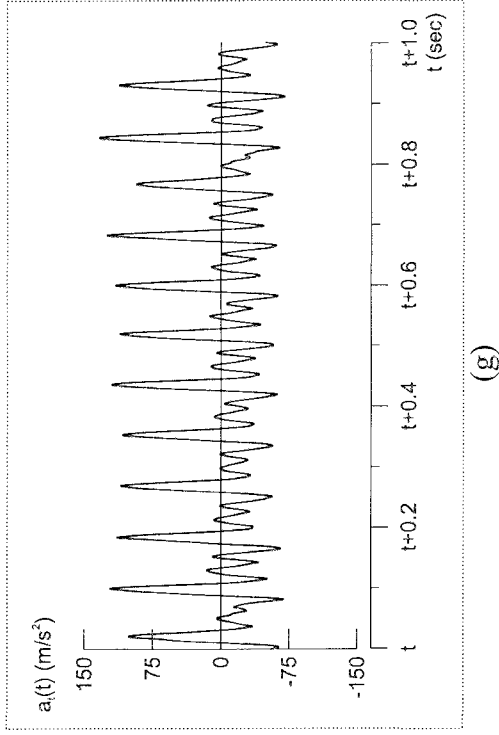
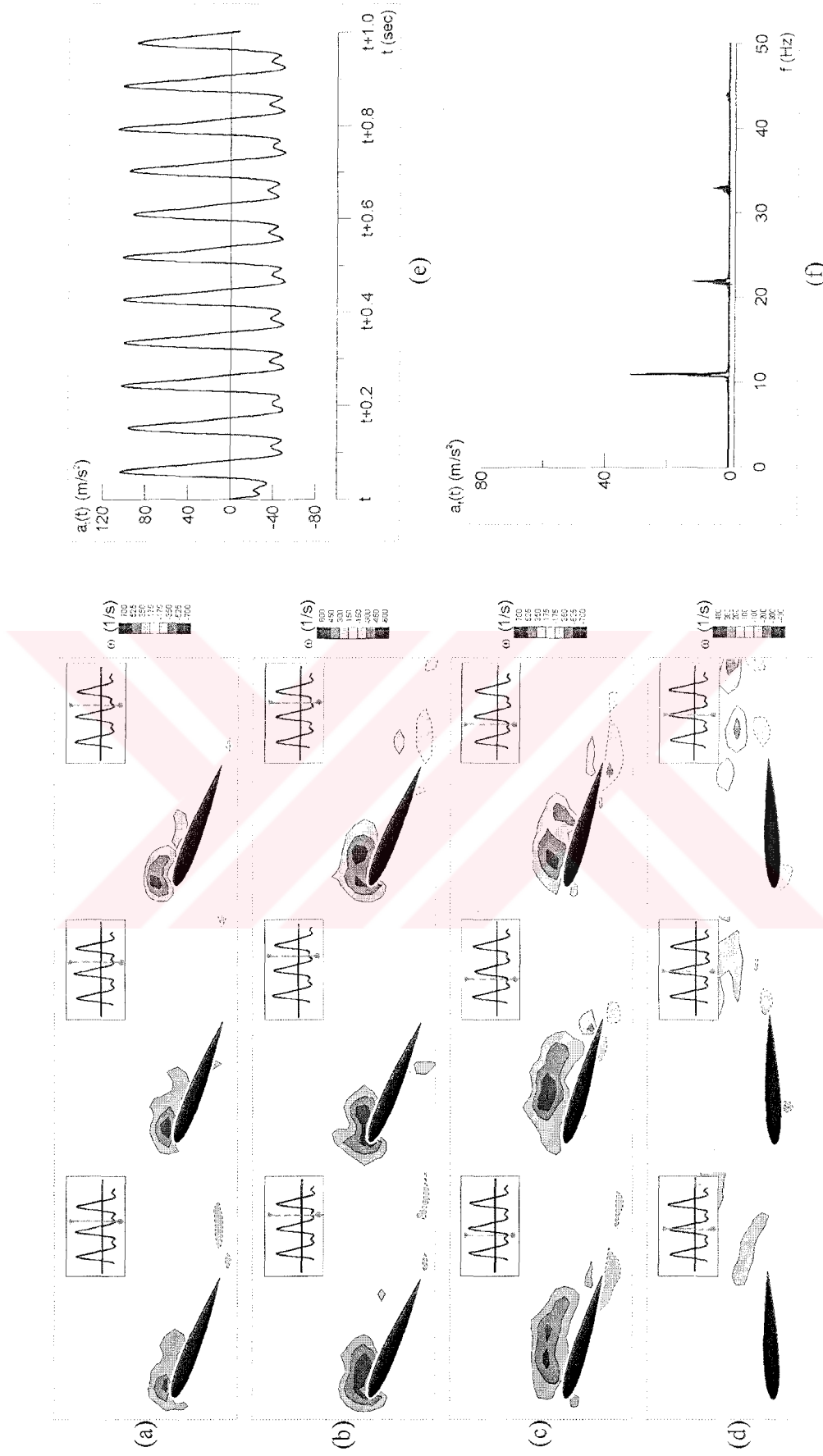


Figure B2.4 Selected 3 images of vorticity patterns for oscillations at $Re = 147,869$ with Spring 2 ($\alpha_{init} = \text{Angle } 2$)

a) $\alpha_{inst} = 8^\circ$ b) $\alpha_{inst} = 10^\circ$ c) $\alpha_{inst} = 12^\circ$ d) $\alpha_{inst} = 14^\circ$ e) $\alpha_{inst} = 15^\circ$ f) $\alpha_{inst} = -1^\circ$
and corresponding acceleration - time trace (g) and acceleration spectra (h) graphs.





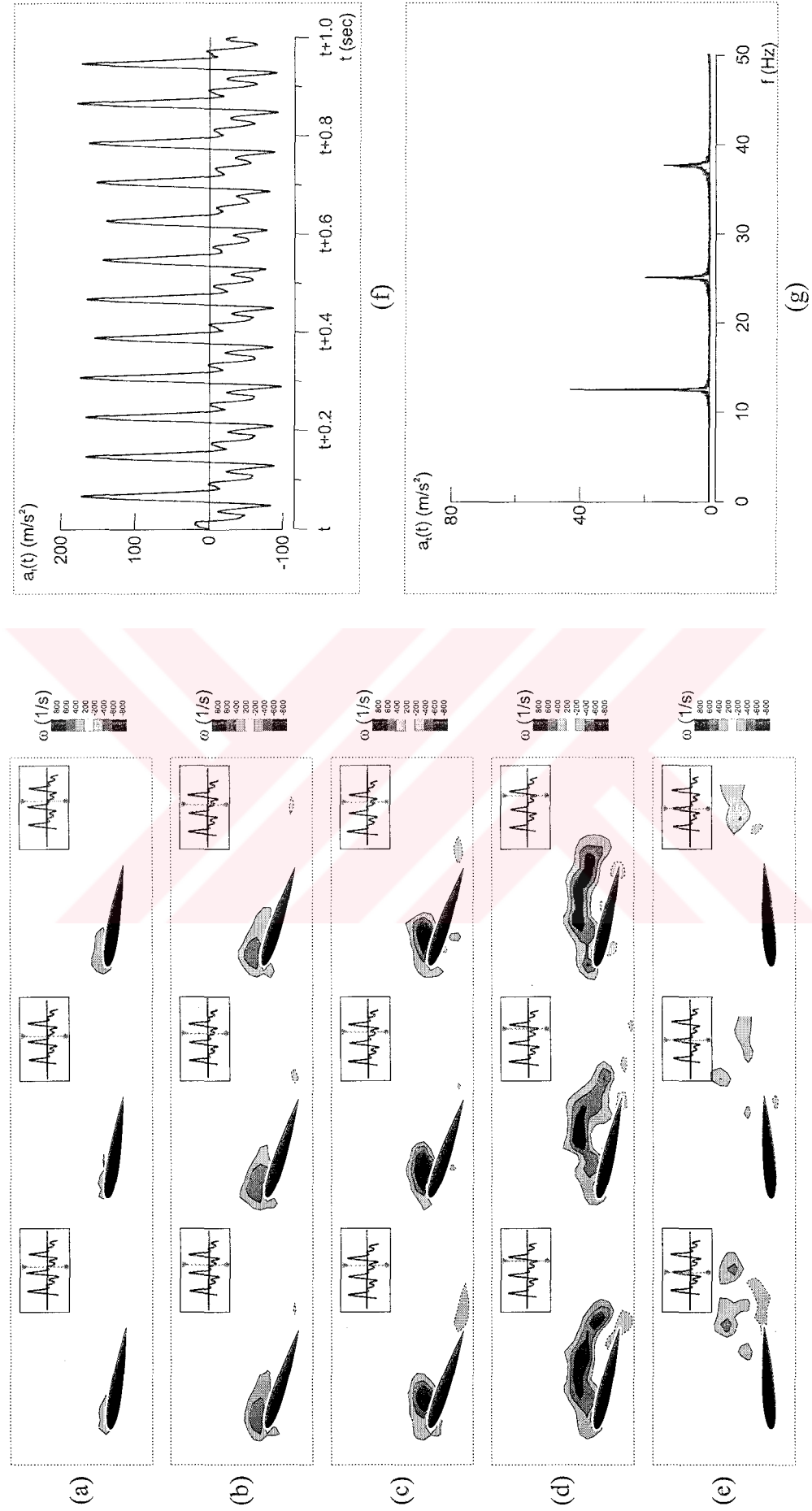


Figure B2.6 Selected 3 images of vorticity patterns for oscillations at $Re = 110,762$ with Spring 3 ($\alpha_{init} = \text{Angle } 2$)

a) $\alpha_{inst} = 10^\circ$ b) $\alpha_{inst} = 18^\circ$ c) $\alpha_{inst} = 19^\circ$ d) $\alpha_{inst} = 13^\circ$ e) $\alpha_{inst} = -4^\circ$
and corresponding acceleration - time trace (f) and acceleration spectra (g) graphs.

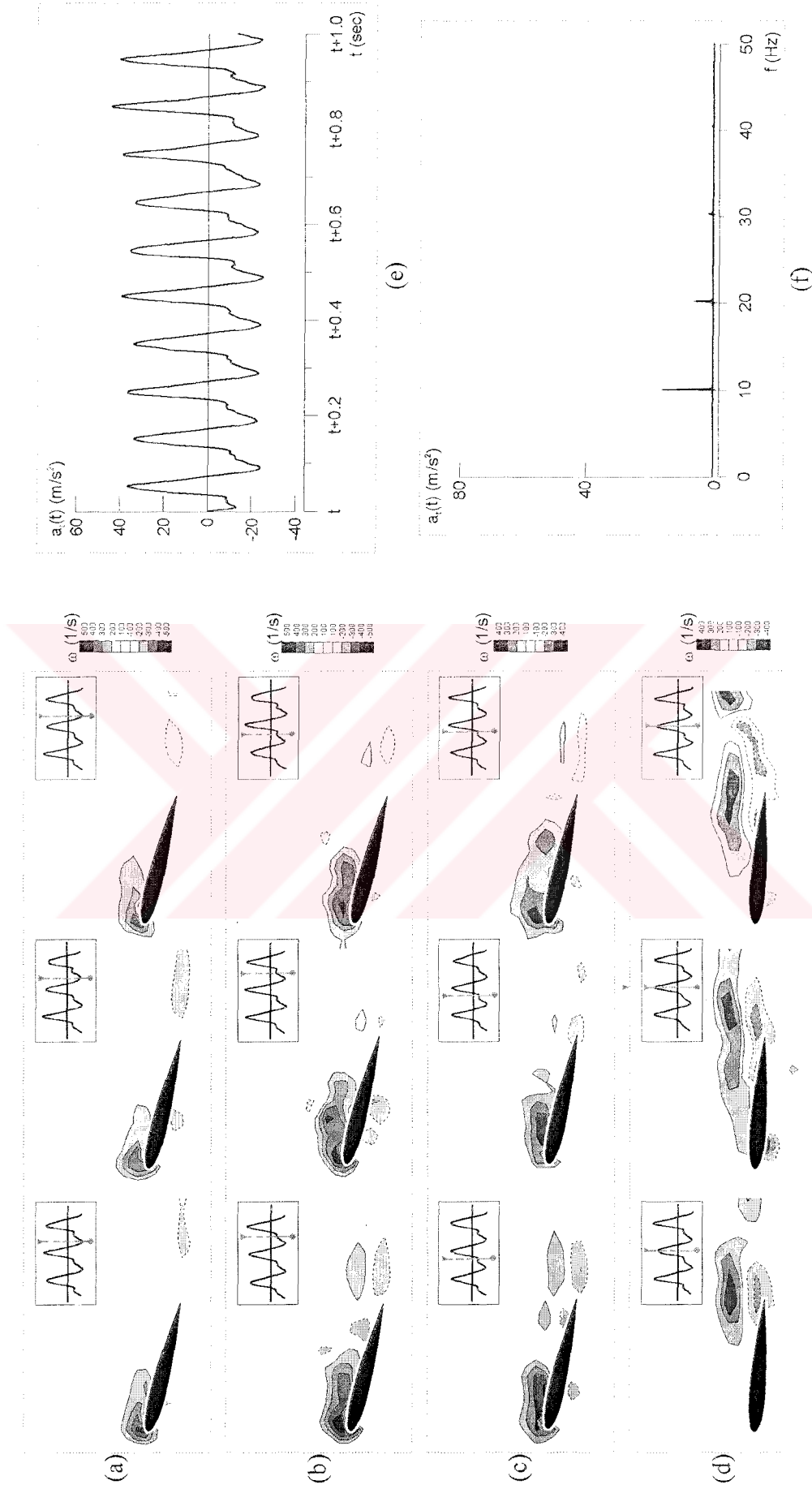


Figure B2.7 Selected 3 images of vorticity patterns for oscillations at $Re = 76,063$ with Spring 3 ($\alpha_{\text{nrt}} = \text{Angle 1}$)

a) $\alpha_{\text{inst}} = 14^\circ$ b) $\alpha_{\text{inst}} = 15^\circ$ c) $\alpha_{\text{inst}} = 12^\circ$ d) $\alpha_{\text{inst}} = 4^\circ$
and corresponding acceleration - time trace (e) and acceleration spectra (f) graphs.

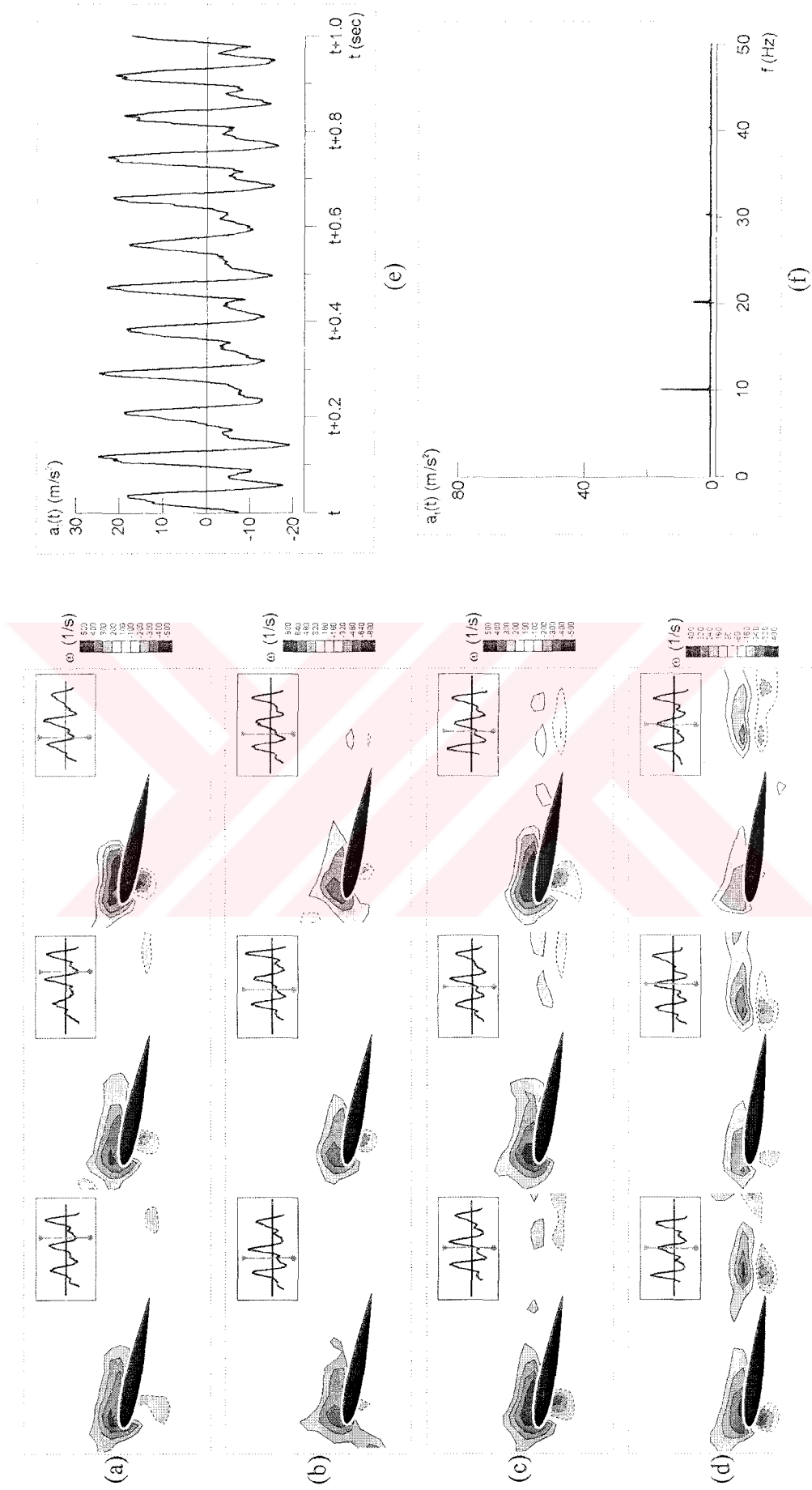


Figure B2.8 Selected 3 images of vorticity patterns for oscillations at $\text{Re} = 110,072$ with Spring 3 ($\alpha_{\text{init}} = \text{Angle 1}$)

a) $\alpha_{\text{inst}} = 11^\circ$ b) $\alpha_{\text{inst}} = 12^\circ$ c) $\alpha_{\text{inst}} = 10^\circ$ d) $\alpha_{\text{inst}} = 7^\circ$
and corresponding acceleration - time trace (e) and acceleration spectra (f) graphs.

APPENDIX B3

VORTICITY FORMATION AROUND THE AIRFOILS FOR ONE PERIOD OF OSCILLATION AND CORRESPONDING INSTANTANEOUS ACCELERATION OF THE AIRFOILS



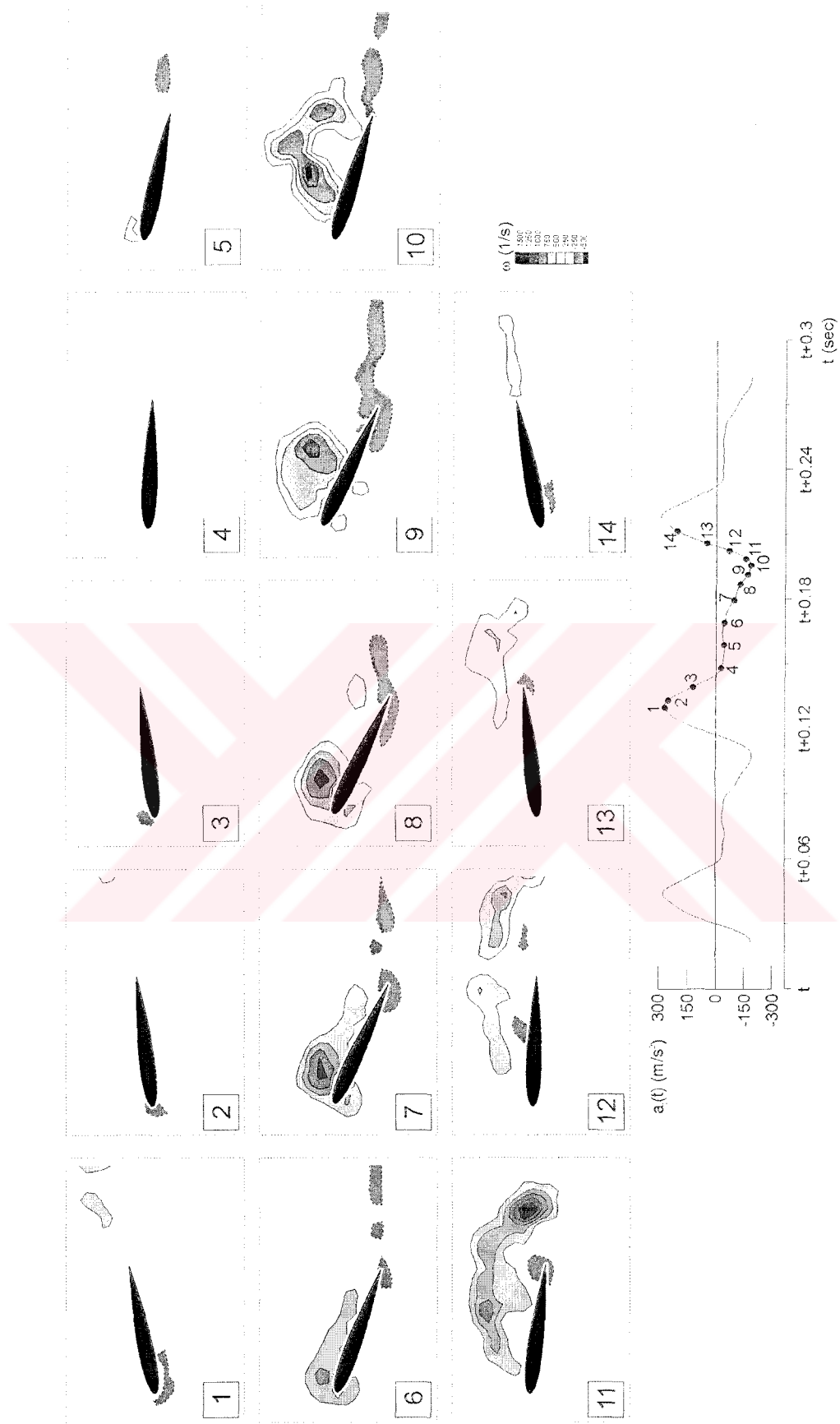


Figure B3.1 Vorticity formation around the airfoil for one period of oscillation and corresponding acceleration of the airfoil, at $Re=145976$, Spring 1, Angle 3. Numbers at the left bottom corners of the images and the corresponding numbers on the acceleration graph indicate the instant when the image is taken.

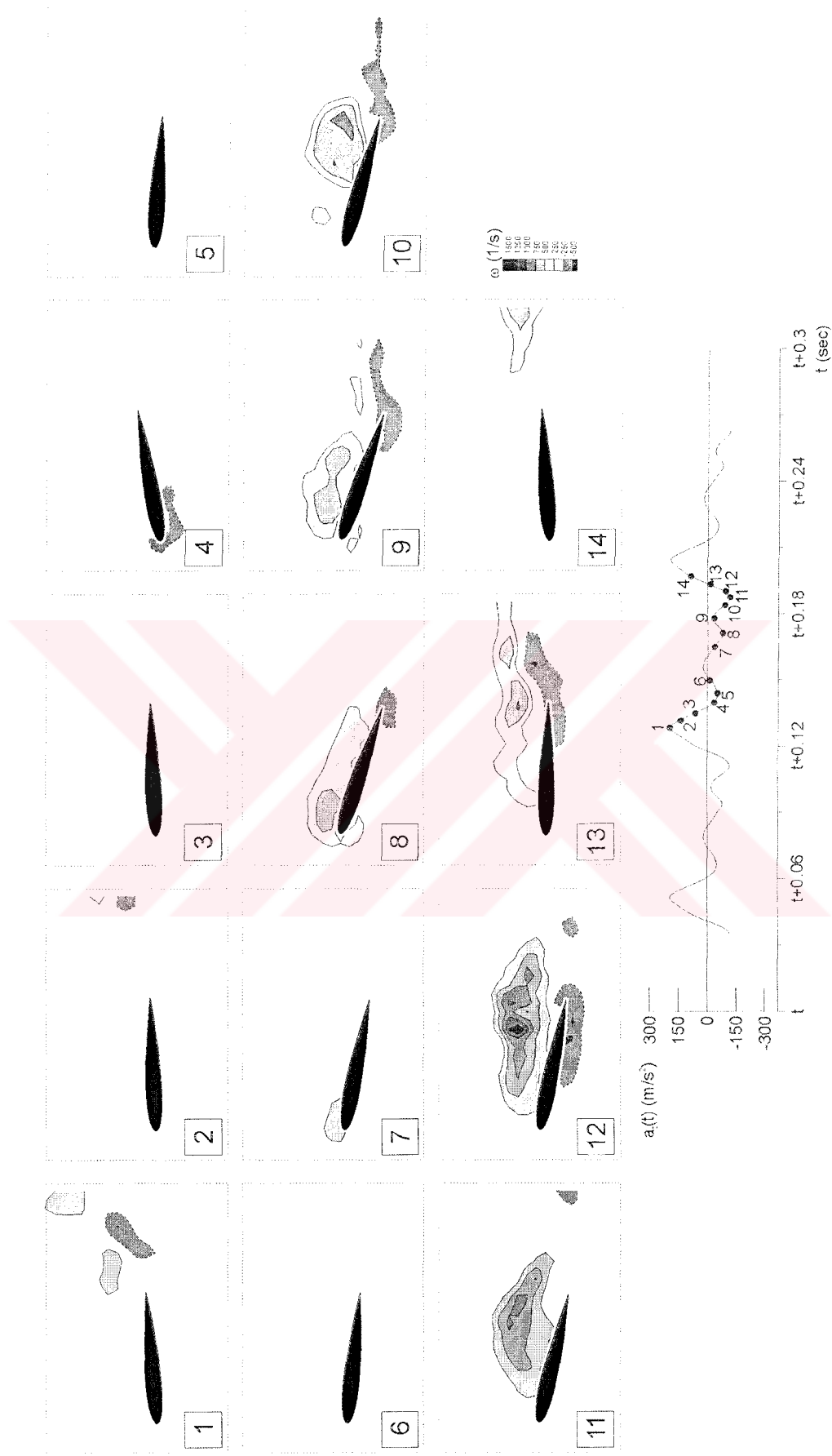


Figure B3.2 Vorticity formation around the airfoil for one period of oscillation and corresponding acceleration of the airfoil, at $Re=141981$, Spring 2, Angle 3. Numbers at the left bottom corners of the images and the corresponding acceleration numbers on the acceleration graph indicate the instant when the image is taken.

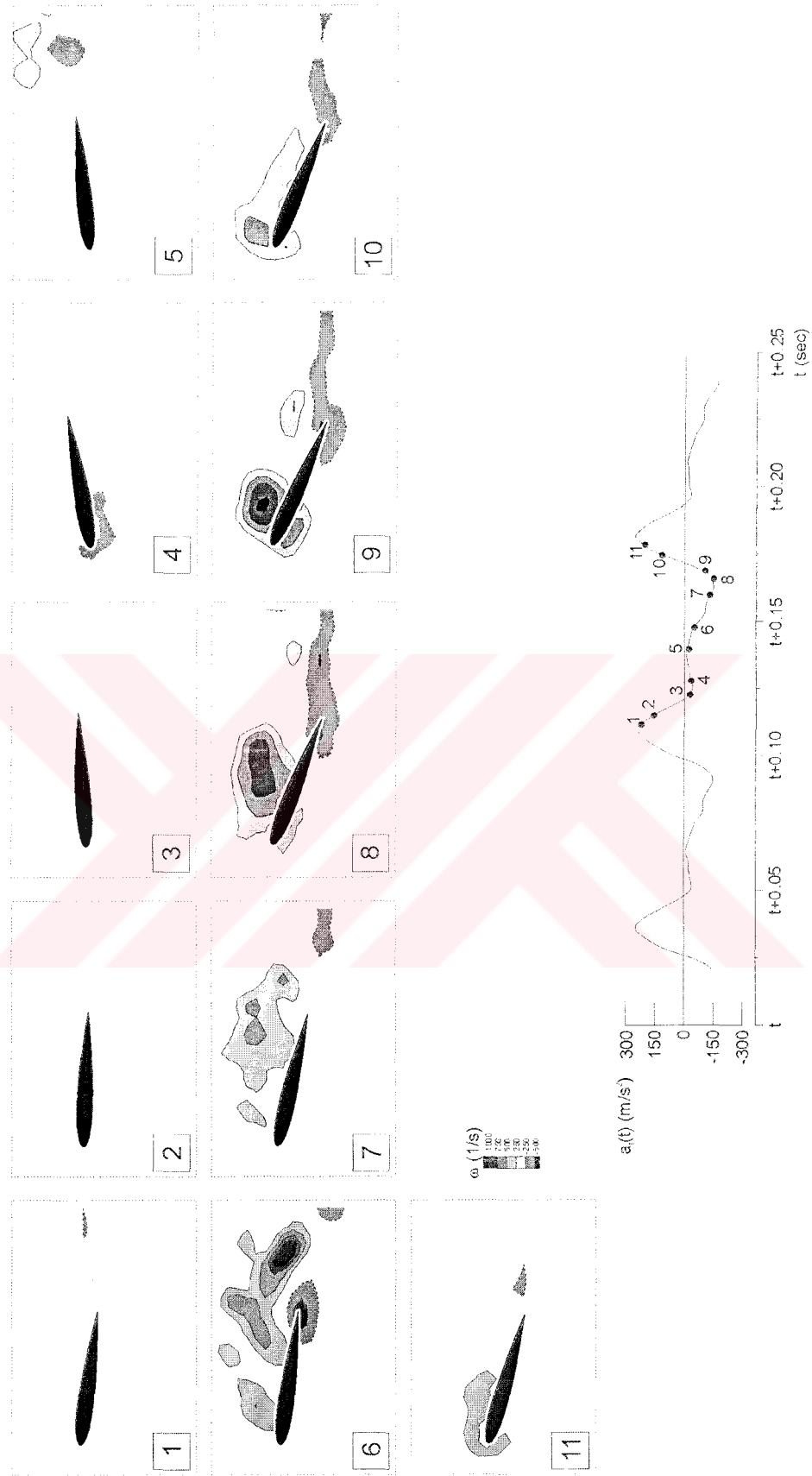


Figure B3.3 Vorticity formation around the airfoil for one period of oscillation and corresponding acceleration of the airfoil, at $Re=144650$, Spring 3, Angle 3. Numbers at the left bottom corners of the images and the corresponding acceleration numbers on the acceleration graph indicate the instant when the image is taken.

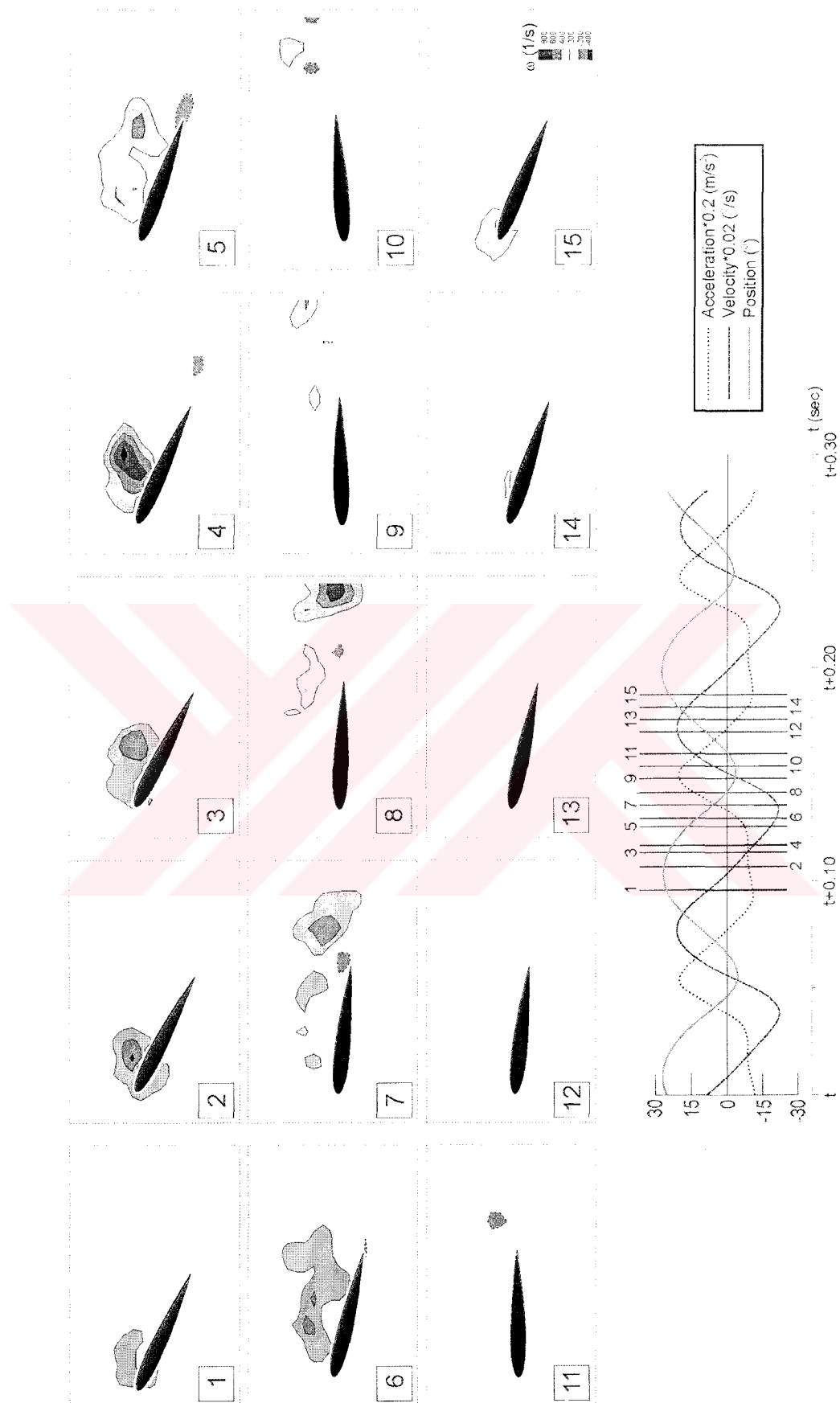


Figure B3.4 Vorticity formation around the airfoil for one period of oscillation at $Re=75189$, Spring 1, Angle 2 and corresponding acceleration, velocity and the displacement of the airfoil

CURRICULUM VITAE

Egemen Tinar was born in Malkara (Tekirdağ) – TURKEY on April 23, 1979. He graduated from Tekirdağ Anatolian High School in 1997. He obtained his B.Sc. degree from Istanbul Technical University, Faculty of Aeronautics and Astronautics, Department of Astronautical Engineering in 2002. Same year he started to M.Sc. program in Aerospace Engineering of the Institute of Science and Technology at Istanbul Technical University. He has been working as a Research Assistant at the Trisomic Research Center since December 2002.

